Article

Large-Scale Model Tests on the Performance and Mechanism of Vertical-Inclined-Piles Wall (VIPW) Structure Upon Excavation

Haozhen Yue * , Yapeng Zhang , Chaoyi Sun , Yun Zheng , Demin Xue

Posted Date: 20 March 2026

doi: 10.20944/preprints202603.1636.v1

Keywords: foundation pit excavation; model tests; support structure; inclined-piles; deformation; settlement; bending moment; axial force

doi:10.20944/preprints202603.1636.v1

Article

Large-Scale Model Tests on the Performance and Mechanism of Vertical-Inclined-Piles Wall (VIPW) Structure Upon Excavation

Haozhen Yue [1,2,*], Yapeng Zhang [3], Chaoyi Sun [4], Yun Zheng [4] and Demin Xue [1,2]

[1] Zhejiang Institute of Communications, Hangzhou 311112, China
[2] Zhejiang Engineering Research Center of Digital Highway Application Technology, Hangzhou 311112, China
[3] Zhejiang College of Construction, Hangzhou 311231, China
[4] State Key Laboratory of Geomechanics and Geotechnical Engineering Safety, Institute of Rock and Soil Mechanics, Chinese Academy of Sciences, Wuhan, Hubei 430071, China
* Correspondence: haozhenyue@zjvtit.edu.cn; Tel.: +86-158-6377-6567

Abstract

With the acceleration of urbanization, numerous deep and large foundation pit projects have been emerging. This paper proposes a new type of support structure for deep foundation pits, namely vertical-inclined-piles wall (VIPW). Six sets of large-scale model tests of foundation pit excavation under 1-g condition were carried out, among which one set was supported by soldier pile wall (SPW) and the other five by VIPW. By monitoring and analyzing the distribution and variation characteristics of vertical pile deformation, surface settlement, pile bending moment, and inclined pile top axial force during the excavation process, the action mechanism of VIPW was revealed, and it was verified that VIPW exhibits better support performance than SPW. Furthermore, four key parameters, including the embedded depth of inclined piles, the inclination angle of inclined piles, the support position of inclined piles, and the embedded depth of vertical piles, were changed respectively to study their influences on the deformation and force characteristics of VIPW, providing a theoretical basis for structural optimization design. Moreover, by comparing the instability and failure characteristics of the foundation pit, it is proved that VIPW can effectively ensure the stability of the foundation pit.

Keywords: foundation pit excavation; model tests; support structure; inclined-piles; deformation; settlement; bending moment; axial force

---

1. Introduction

With the rapid urban development, ground space tends to be saturated, and cities become more and more crowded. More high-rise buildings and large underground projects appear to solve population, resource and environmental problems. Thus, many large scale deep foundation pits are constructed in dense urban areas. Construction of excavations causes ground stress redistribution and soil movement, which may impact on proximity structures [1,2]. Inappropriate retaining method and excavation process can result in adjacent buildings becoming damaged and even produce casualties, which poses a serious threat to the life safety and property of the on-site workers and surrounding residents [3–5].

To control the deformation during the excavation process and ensure construction safety, a series of retaining and protection measures have been developed and adopted, including retaining structures, anchors and struts [6,7]. Thus, cantilever retaining structure, anchored retaining structure and strutted retaining structure, are the most popular retaining and protection methods for excavations in practice [8]. Many scholars have studied their performance and mechanisms. Yu et al.

[9] studied the bending moment of diaphragm wall, surface settlement and tunnel deformation by centrifugal model test and numerical simulation. He conducted that the diaphragm walls present convex deformation towards foundation pit, and the surface settlement outside the diaphragm wall appears to be the concave groove type. Yi et al. [10] analyzed a progressive collapse incident in a propped excavation through 2D and 3D simulations. It is found that inconsistent strut elevations caused excessive bending in the connecting capping beam, leading to its fracture and the subsequent overturning failure of the corner section. In-situ monitoring and numerical methods were employed by Wang et al. [11] to investigated the composite soil nailing wall-anchored soldier pile wall retaining system, finding that retaining piles' bending moment and lateral displacement extremums rise with excavation depth. Increasing retaining pile rigidity/embedded depth or anchor prestress controls lateral displacement effectively within a certain range, with negligible control effectiveness beyond it. Mao et al. [12] compared the protective effects of pile-anchor and double-row pile support via scaled model tests and numerical simulations, and found pile-anchor support markedly superior for controlling soil deformation and reducing subway disturbances in loess area foundation pit excavation adjacent to subways, which is preferable if conditions allow.

However, these retaining structures have the following shortcomings. For example, in internal bracing retaining structures, the local failure of several struts may occur, which causes the bracing axial forces to transfer to adjacent struts, induces further strut failure, and ultimately leads to the instability and subsequent failure of the foundation pit [2,13]. Meanwhile, for large-scale foundation pit projects, the use of internal bracings is both costly and time-consuming [14]. For anchor bolt (cable) support, it does not occupy the inner pit space and facilitates earth excavation within the foundation pit. However, its reliability is relatively low, thus leading to a relatively high level of construction risk [15,16].

At present, many new types of retaining and protection for excavations have been invented and studied through numerical simulation, engineering case application, field monitoring and large-scale model tests。These retaining measures are designed to control foundation pit deformation and cut down construction costs through the adjustment of the form of internal bracing for foundation pits. Zheng et al. [17–21] proposed converting part of the vertical piles into inclined piles. They investigated various excavation retaining structures including the inclined framed retaining wall (IFRW), the inclined-vertical framed retaining wall (IVFRW), and the inclined alternating combination steel pipe pile retaining structure (IACSPPRS). Wang et al. [22] adopted finite element simulation to investigate the deformation mechanism of soil mass during foundation pit excavation under the action of the inclined pile retaining structure, particularly the displacement distribution law of the soil between piles and the soil inside and outside the foundation pit. Xie et al. [23] systematically investigated the deformation characteristics, mechanical mechanism and stability of the IFRW under excavation and overload conditions by adopting a combined approach of field tests and numerical simulations. Zhang et al. [24] proposed to design inclined piles directly in the pit and provide their support at a suitable position below the top of vertical piles. As shown in Figure 1, this supporting structure mainly increases its rigidity by optimizing the form of the internal support structure. However, they only adopted numerical simulation to study its performance. Systematic studies on VIPW are rarely reported, and more experimental data are urgently needed for a better understanding of the performance and working mechanism of VIPW during foundation pit excavation.

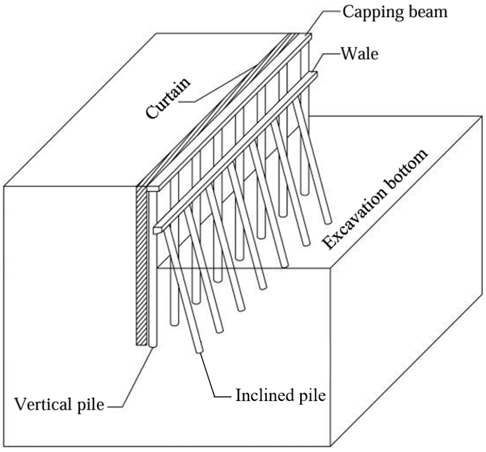

Figure 1. Basic configuration of the VIPW.

In this study, a series of 1-g experimental model tests were carried out to investigate the performance and working mechanism of VIPW. In the experiment, the laser displacement sensors, resistance strain gauge and micrometer were arranged to record the whole excavation process. The influence on the supporting effect is studied by changing the inclination angle, the length of inclined pile, and the supporting position. Particle image velocimetry(PIV)technology was also employed to explore the soil movements behind the vertical piles. The deformation and bending moment distribution of the vertical piles, surface settlement and soil movements behind the vertical piles, bending moment distribution of the inclined piles were discussed in detail. The findings would be potentially important for the practical use of herringbone retaining structure in the future large scale-deep excavation constructions.

2. Model Tests of VIPW

2.1. Scaling Ratio of the Models

The full VIPW consists of vertical piles, batter piles, capping beam and wale [24]. The vertical piles are distributed along the edge of the excavation for resisting the earth pressure acting on their backs, and they are mainly subjected to bending moment load. Thus, the bending stiffness *EI* is the significant parameter of vertical piles for reflecting their lateral bearing capacity [25]. The inclined piles are built inside the excavation and are linked to the vertical piles via the wale. They provide support axial force to limit the horizontal displacement of the vertical piles. Thus, the compressive stiffness *EA* is the significant parameter of inclined piles for reflecting their compressive deformation capacity. The capping beam and wale were located on the top and at a certain depth below ground surface, respectively. The beam is used to increases vertical piles' integrity. The wale is used to link the vertical piles and inclined piles together and transfers some of the load acting on the vertical piles to the inclined batter piles. The capping beam and wale are not the main structures to limit the deformation. Therefore, their model material only needs to meet a certain strength and take geometric similarity into account.

In this paper, the geometric dimensions and mechanical parameter of VIPW model were reasonably determined through the similarity of bending stiffness *EI* and the compressive stiffness *EA* principle respectively. Table 1 shows the values of main scaling ratios of 1-g model test.

Considering the excavation scale and model test equipment size, the geometric similarity ratio of the model test was $C_l = 20$. The gravitational acceleration of the model is consistent with that of the prototype. Therefore, the similarity ratio C_g of gravitational acceleration g is equal to 1.

Due to the difference of the soil void ratio between the model and the prototype, the density similarity ratio C_ρ at the reference point is not equal to the geometric similarity ratio C_l. However, the density difference of the reference point soil layer between the model and the prototype is so small that it can be ignored. Thus, it can be considered that the density similarity ratio $C_\rho = 1$ [26,27]. According to the similarity criterion, the similarity ratio of each physical quantity can be calculated.

Table 1. The main scales relations of 1-g physical modelling in tests (prototype/model).

Quantity to be scaled	Scaling factor	Prototype to model ratio	Quantity to be scaled	Scaling factor	Prototype to model ratio
Length	C_l	20	Cohesion	$C_c = C_l C_\rho C_g$	20
Density	C_ρ	1	Friction angle	C_φ	1
Mass	$C_m = C_l^3 C_\rho$	20^3	Force	$C_F = C_l^3 C_\rho C_g$	20^3
Gravitational acceleration	C_g	1	Poisson's ratio	C_v	1
Stress	$C_\sigma = C_l C_\rho C_g$	20	Strain	C_ε	1
Area	$C_A = C_l^2$	20^2	Bending moment	$C_M = C_l^4 C_\rho C_g$	20^4
Inertia moment	$C_I = C_l^4$	20^4	Young's modulus	$C_c = C_l C_\rho C_g$	20
Bending stiffness	$C_{EI} = C_l^5 C_\rho C_g$	20^5	Compressive stiffness	$C_{EA} = C_l^3 C_\rho C_g$	20^3

2.2. Experimental Program and Set Up

2.2.1. The Large-Scale Model Platform of Combined Steel Structure

The model tests were conducted in the model box made of steel. The size of test model box is 2.4m × 1m × 1.8m (length × width × height)(see Figure 2). Clear plexiglass with thickness of 2 cm is installed on one side of the model box to facilitate observation and record the test process. The model box was polished internally to minimize the side friction that may be developed between the container and the soil.

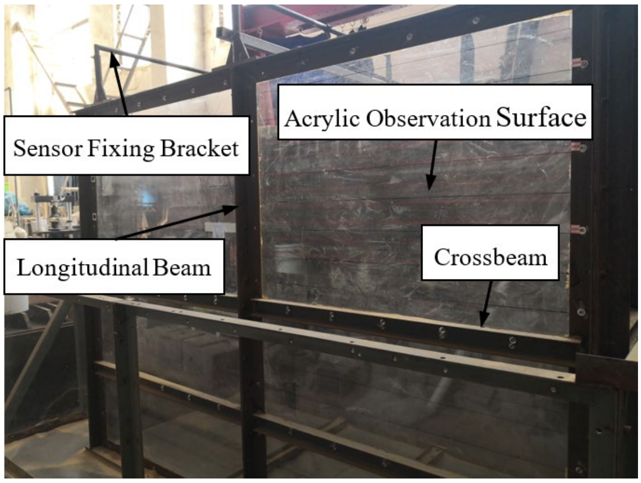

Figure 2. Model box.

2.2.2. Excavation-Supported System

The model piles, including vertical piles and inclined piles, were fabricated from round PVC pipes(see Figure 3). The outside diameter of the vertical pile is 50 mm, and the wall thickness is 2 mm. The outside diameter of the inclined pile is 40 mm, and the wall thickness is 2 mm. The length of the model piles are designed according to Table 5 and Figure 11 below.

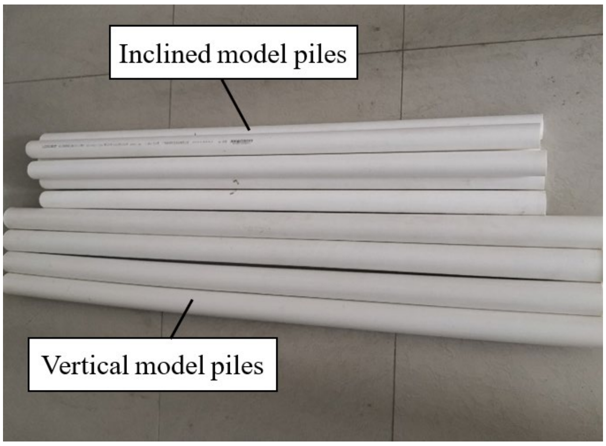

Figure 3. Pile models.

Uniaxial compression tests were carried out on two kinds of PVC pipes, in order to obtain their Young’s modulus(see Figure 4). The height to diameter ratio of the PVC plastic pipe specimen is 2, which can reduce the end effect of the specimen(see Table 2). Displacement control method was used in these tests. Figure 5 shows the axial stress-strain relationship curve of PVC plastic pipe. It is noticed from the figures that there are obvious linear elastic deformation stages in the stress - strain curves. Model piles are subjected to limited load during excavations in the tests. Thus, it can be considered that the piles are in the elastic deformation stage. According to the experimental results, the Young’s modulus (E) of PVC pipes used in the model tests is calculated according to the following formula [28,29].

$$E = max \frac{\sigma_A - \sigma_B}{\varepsilon_A - \varepsilon_B} \quad (1)$$

where σ_A and σ_B are the stress corresponding to Point A and Point B on the stress-strain curve, respectively. ε_A and ε_B are the strain of Point A and Point B, respectively.

σ_A and σ_B are assumed to obey the following equation:

$$\sigma_A - \sigma_B = 50\%\sigma_0 \quad (2)$$

where σ_0 is the peak stress.

Table 2 shows the Young’s modulus of pile models calculated according to Equation (1) and Equation (2). Thus, the bending stiffness(EI) of vertical pile model is 286.3 N·m2, as the pile with a diameter of 1 m, and bending stiffness(EI) of 9.16×105 kN·m2 in prototype. The compressive stiffness(EA) of inclined pile model is 6.8×105 N, as the pile with a diameter of 0.8 m, and compressive stiffness(EA) of 5.44×109 N in prototype.

Capping beam, wale and the connection between them mainly transfer load between vertical piles and inclined piles. Thus, they are made of stainless steel material regardless of their material similarity. The section shape of capping beam, wale is rectangular, with height of 40 mm, width of 20 mm, and length of 980 mm. Capping beam, wale, vertical piles and inclined are installed according to Figure 6. Figure 7 is the photos of capping beam, wale, and the connection.

doi:10.20944/preprints202603.1636.v1

Figure 4. Uniaxial compression test of pile model.

Table 2. Young's modulus (E) of pile models.

Number	Dameter(mm)	Thickness (mm)	Height (mm)	Young's modulus(GPa)	Average Young's modulus(GPa)
Z1	50	2.0	97.0	3.16	3.29
Z2	50	2.0	96.4	3.37	
Z3	50	2.0	97.0	3.35	
X1	40	2.0	76.7	2.83	2.85
X2	40	2.0	76.3	2.79	
X3	40	2.0	76.7	2.94	

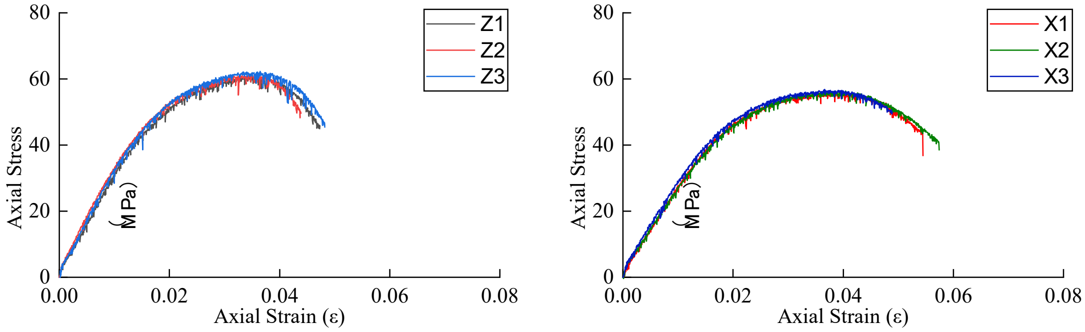

(**a**) (**b**)

Figure 5. Stress-strain curve of pile model: (**a**) Vertical model piles; (**b**) Inclined model piles.

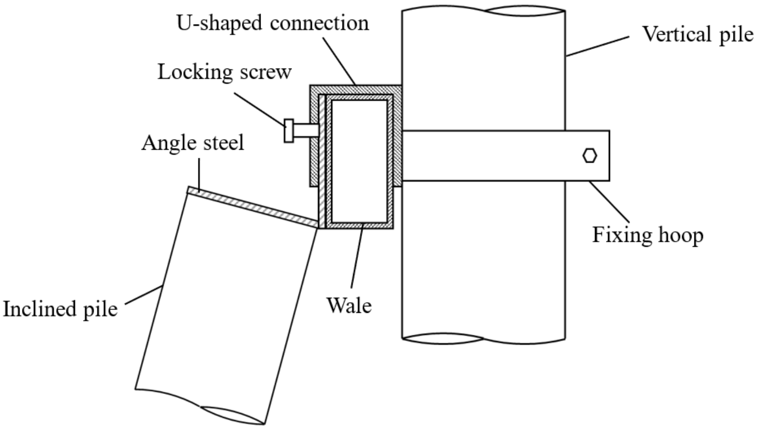

doi:10.20944/preprints202603.1636.v1

Figure 6. Diagram of connection between vertical pile and inclined pile.

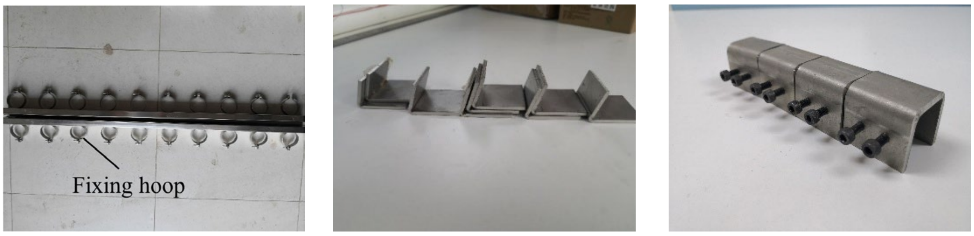

(**a**) (**b**) (**b**)

Figure 7. Wale model and connector: (**a**) Wale; (**b**) Angle steel; (**c**) U-shaped connection.

In order to simulate the soil retaining effect of vertical piles and shotcrete between them, polyester (PET) film with thickness of 0.038mm was pasted on the back side of model piles to prevent sand leakage from the cracks between piles. The impact of PET film on the flexural stiffness of vertical piles can be ignored.

2.2.3. Soil Preparation

The model tests were performed in dry sand. Table 3 presents the particle size distribution of the soil. The coefficient of the nonuniformity C_u is 1.81, and the coefficient of curvature C_s is 0.88. The grain size d50 is less than 0.5 mm. $D_v/ d_{50} > 100$ and $D_i/ d_{50} > 80$, where D_v is the diameter of vertical pile and Di is the diameter of inclined pile. Thus, the grain-size effect can be ignored. Table 4 presents the main physical and mechanical parameters of the soil。

Table 3. Particle size distribution of the soil.

Particle size (mm)	2	0.5	0.25	0.075	0.005
The mass percentage of particles smaller than a specified particle size(%)	100	59.8	0.9	0	0

Table 4. Physical and mechanical parameters of the soil.

Soil type	ω	ρ_{dmax}(g/cm^3)	ρ_{dmin}(g/cm^3)	G_s	φ(°)	c(kPa)
Medium sand	0.1%	1.66	1.45	2.66	38.8	0

Note: ω = water content of soil; ρ_{dmax} = maximum dry density of soil; ρ_{dmin} = minimum density of soil; G_s= specific gravity; φ = internal friction angle of soil; c = cohesion of soil.

2.2.4. Monitoring Program

In order to better understand the performance of VIPW during foundation pit excavation, a series of instruments were installed in each group of experimental models, including dial indicator for monitoring horizontal displacement of vertical pile (see Figure 8a), compact laser displacement sensor for monitoring settlement (see Figure 8b), and strain acquisition system for monitoring strain of piles (see Figure 9).

(**a**) (**b**)

Figure 8. Photo of displacement sensors: (**a**) Dial indicator; (**b**) Compact laser displacement sensor.


(**a**) (**b**)

Figure 9. Strain acquisition system: (**a**) Strain gauge; (**b**) Strain acquisition instrument.

Z6 is the monitoring vertical pile for horizontal displacement and Z4, Z5 and Z7 are the monitoring vertical piles for strain in Groups R0-R5, respectively. X4 to X6 are the monitoring inclined piles for strain in Groups R1–R5. Compact laser displacement sensors are installed above the ground surface behind the vertical piles. Figure 10 shows the Sensor layout of test model.

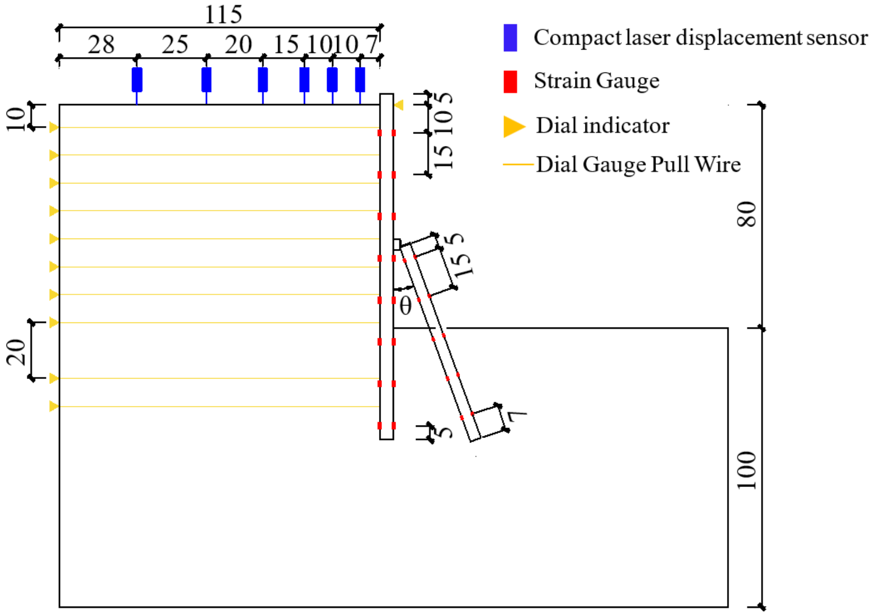

Figure 10. Sensor layout of test model (unit: cm).

2.3. Test Scheme

Different retaining structures, including VIPW and soldier pile wall (SPW), were employed in the model tests. Figure 11 shows the arrangement of VIPW model. The arrangement of SPW is the same as that of vertical piles in VIPW model. Table 5 list the test scheme in this paper. Excavation in Group R0 is protected by SPW, whereas those in Groups R1–R5 use VIPW. The center–center spacing of the vertical piles is 10 cm, i.e., twice their diameter. The inclined piles lie in between each pair of adjacent vertical piles with center–center spacing of 10 cm (see Figure 11b).

The excavation process is divided into two stages. Firstly, sand is removed from ground level to the position of wale (H1). There is no connection between the inclined pile and the wale, and no force is transferred between them in this stage. The inclined piles are then linked to the wale, and the excavation is continued until the foundation bottom in the second stage.

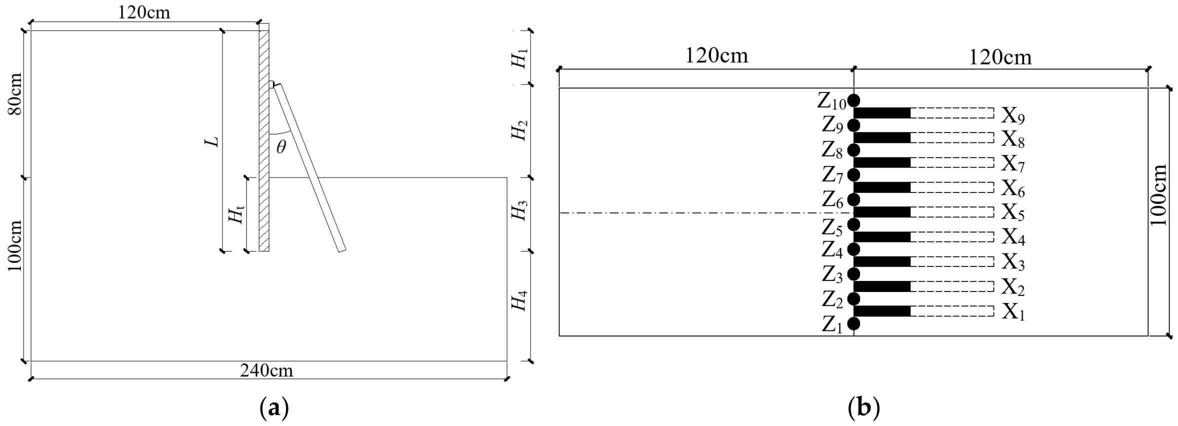

(**a**) (**b**)

Figure 11. Strain acquisition system: (**a**) Sectional view; (**b**) Plan view. H_t = depth from the excavation bottom to the tip of vertical pile; L= length of vertical pile; L_x= length of inclined pile; θ= dip angle of inclined pile; H_1 = depth from the wale to the ground surface; H_3 = depth from the excavation bottom to the tip of inclined pile; Z_1 to Z_{10} are the ten vertical piles distributed along the edge of the excavation, with a center-to-center spacing of 10 cm; X_1 to X_9 are the nine inclined piles tilting to the inner side of the excavation, with a center-to-center spacing of 10 cm.

Table 5. Experimental scheme.

Number	H_t(cm)	L(cm)	L_x(cm)	θ(°)	H_1(cm)	H_3(cm)
R0	80	120	-	-	-	-
R1	80	120	72	15	50	40
R2	80	120	82	15	50	49.6
R3	80	120	74	20	50	40
R4	80	129.6	72	15	50	40
R5	80	120	83	15	40	40

2.4. Test Procedures

2.4.1. Preparation of Model Piles

Model piles are manufactured according to Table 5. A half-bridge circuit is realized by a pair of strain gauges symmetrically pasted on both side of the vertical model pile. Thus, the bending strain of the vertical model piles can be recorded through several pairs of strain gauges at a distance of 15 cm along the pile shaft, as shown in Figure 12(a). The internal force distribution of inclined pile is complicated, and its strain is affected by both axial force and horizontal force. Therefore, a pair of strain gauges are pasted perpendicularly to each other at each monitoring point to form a half-bridge circuit on one side of the inclined model pile. And several half-bridge circuits symmetrically pasted on both side at a distance 15 cm along the inclined pile shaft (X4 to X6), as shown in Figure 13(a). As a result, the strain of each monitoring point before and behind the pile can be recorded during excavations. The surface of the strain gauges is coated with room temperature-vulcanized silicone rubber (see Figure 12(b) and Figure 13(b)).

The surface of the PVC pipe is relatively smooth. In order to make the strength properties of the pile-soil interface in the tests fit the reality, fine sand is pasted on the surface of the inclined model piles, as shown in Figure 14.

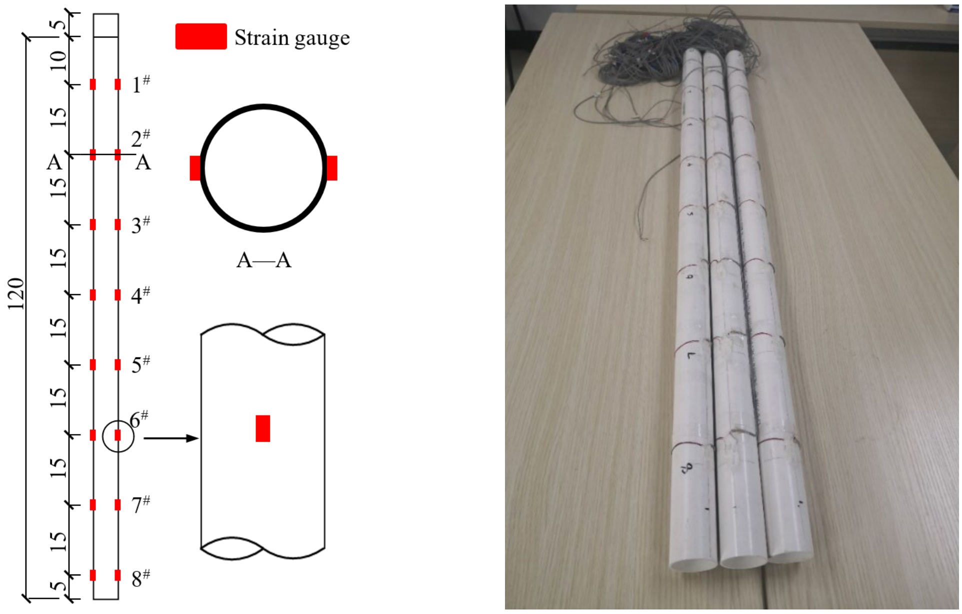

(**a**) (**b**)

Figure 12. Strain gauge arrangement of vertical pile model: (**a**) Strain gauge measuring point layout (Unit: cm); (**b**) Installation status of strain gauges.

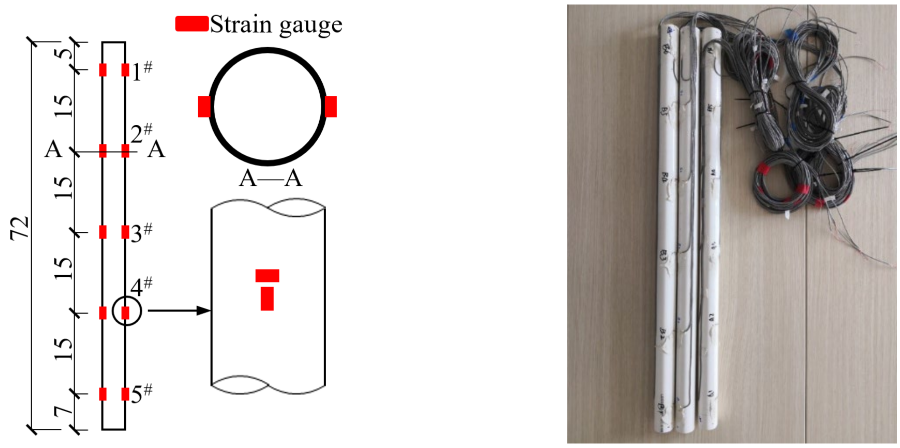

(**a**) (**b**)

Figure 13. Strain gauge arrangement of inclined pile model: (**a**) Strain gauge measuring point layout (Unit: cm); (**b**) Installation status of strain gauges.

Figure 14. Photo of inclined pile model.

2.4.2. Coefficient Calibrating Testing for Strain Gauges on Monitoring Pile

The uncertainty factors, such as the accuracy error of the strain gauge itself and the non-standardization of the pasting process, lead to the difference between the measured value and the real value. Thus, strain gauges were calibrated to get their sensitivity coefficient through simply supported beam loading test. Figure 15 shows the coefficient calibrating testing of vertical piles range from Groups R1–R5. Loads are applied on the middle of the model beam in 7 stages. 4.5 N is loaded at the first stage and 10 N is loaded each time at the remaining stages. The bending moment (M) of each monitoring point is calculated according to the loading weights. Then, the relationship between M and ε_{max} is obtained, and the calibration results of Z4 and X5 model piles in Group R5 tests are taken as examples, as shown in Table 6 and Table 7.

Table 6. Relationship between M and ε_{max} of vertical model piles.

Pile Number	Strain Number	Relationship between M and ε_{max}	Pile Number	Strain Number	Relationship between M and ε_{max}
Z4	$1^{\#}$	$y = 0.0122x(R^2 = 1)$	Z4	$8^{\#}$	$y = 0.0125x(R^2 = 1)$
Z4	$2^{\#}$	$y = 0.0136x(R^2 = 1)$	Z4	$7^{\#}$	$y = 0.0135x(R^2 = 1)$
Z4	$3^{\#}$	$y = 0.0136x(R^2 = 1)$	Z4	$6^{\#}$	$y = 0.0133x(R^2 = 1)$
Z4	$4^{\#}$	$y = 0.0138x(R^2 = 1)$	Z4	$5^{\#}$	$y = 0.0133x(R^2 = 1)$

Table 7. Relationship between M and ε_{max} of inclined model piles.

Pile Number	Strain Number	Relationship between M and ε_{max}	Strain Number	Relationship between M and ε_{max}
X5	A-$1^{\#}$	$y = 0.0067x(R^2 = 1)$	B-$1^{\#}$	$y = 0.0066x(R^2 = 1)$
X5	A-$2^{\#}$	$y = 0.0062x(R^2 = 1)$	B-$2^{\#}$	$y = 0.0065x(R^2 = 1)$
X5	A-$3^{\#}$	$y = 0.0066x(R^2 = 1)$	B-$3^{\#}$	$y = 0.0065x(R^2 = 1)$
X5	A-$4^{\#}$	$y = 0.0069x(R^2 = 1)$	B-$4^{\#}$	$y = 0.0066x(R^2 = 1)$
X5	A-$5^{\#}$	$y = 0.0068x(R^2 = 1)$	B-$5^{\#}$	$y = 0.0066x(R^2 = 1)$
X5	A-$6^{\#}$	$y = 0.0069x(R^2 = 1)$	B-$6^{\#}$	$y = 0.0068x(R^2 = 1)$

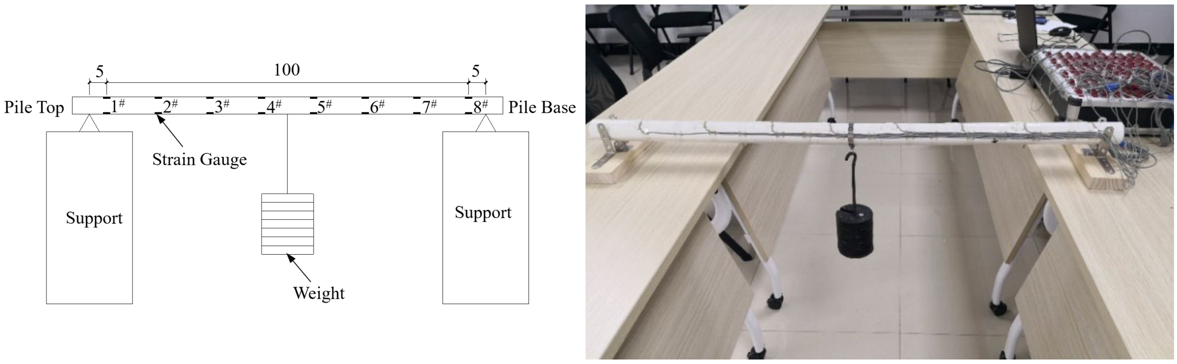

(**a**) (**b**)

Figure 15. Calibration test of pile model: (**a**) Model pile calibration diagram (Unit : cm); (**b**) Model pile calibration photos.

2.4.3. Foundation Soil Preparation and Pile Model Installation

Static testing was carried out to determine the pore ratio of each soil layer. Soil sample was preloaded in the tests, as shown in Figure 16. The loading weight was equal to the stress at the center of each layer in the excavation model. The results showed that the pore ratio of different soil layers after preloading ranges from 0.775 to 0.787, and the density ranges from 1.49 to 1.50 g/cm^3. Thus, it is assumed that the soil in the model is homogeneous, and its density remains as 1.495 g/cm^3。

Sand is poured into model box by layers and pieces with quality control method. "Zero distance" compaction method was used in order to avoid the uneven distribution of sand compactness. That is to say, a tamper is used to fine-tune the sand surface to a defined height to ensure the corresponding porosity and soil layer surface smoothness during each soil layer. The height of each soil layer is 10 cm. The length of the model box is 2.4 m, and its width is 1.0 m. The mass of each layer of soil is 359 kg. The foundation soil stands for 24 hours after filling over, to make it compacted and stable under self-weight.

Figure 16. Static testing.

VIPW model was installed after filling 60 cm of foundation soil (R4 with 50.4 cm). The actual length of the vertical model piles used in the tests are 5 cm longer than the effective pile length (*L*) listed in Table 5. The extra 5 cm length is higher than the ground surface, which is convenient to install the dial indicator on the pile top to monitor the horizontal displacement. Capping beam is installed on the vertical piles, 5 cm below their top. Wale is installed on the vertical piles, with a distance of H_1 below the ground surface. In this process, there is no contact and load transformation between vertical piles and inclined piles. Figure 17(a) shows the VIPW model installation in Group R1. Figure 17(b) is the side view of the model box after filling the sand.

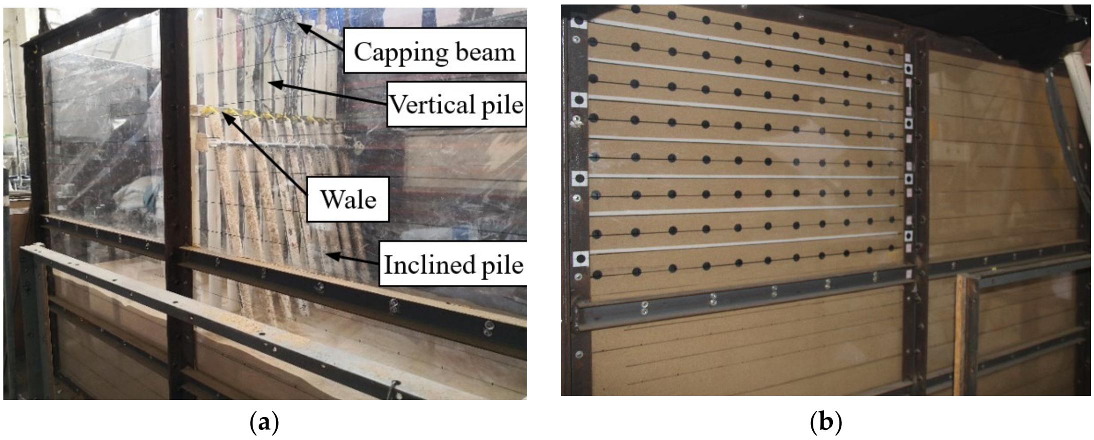

Figure 17. Photos of test model: (**a**) Photo of VIPW model installation in Group R1; (**b**) Photo of the completion of the filling.

2.4.4. Displacement Sensors Installation and Instrumentation Debugging

After finishing filling the foundation soil, 6 laser displacement sensors are installed above the center line of ground surface, and dial indicators are installed on the side and top of the model box to monitor horizontal displacement of vertical pile, respectively, according to Figure. 10. Figure 18 shows the test model after sensor installation.


(**a**) (**b**)

Figure 18. Photos of model after sensor installation: (**a**) Installation of dial indicator; (**b**) Installation of laser displacement meter.

2.4.5. Excavation Process

Sand is removed from the model box in eight stages. Sand of 10 cm thickness is removed at each stage (see Figure 19(a)). When the sand is removed to a depth of H_1, where the wale is installed, followed by installing the connector to link the inclined piles with vertical piles (see Figure 19(b)). After that, excavation is continued until the bottom is reached (see Figure 19(c)).

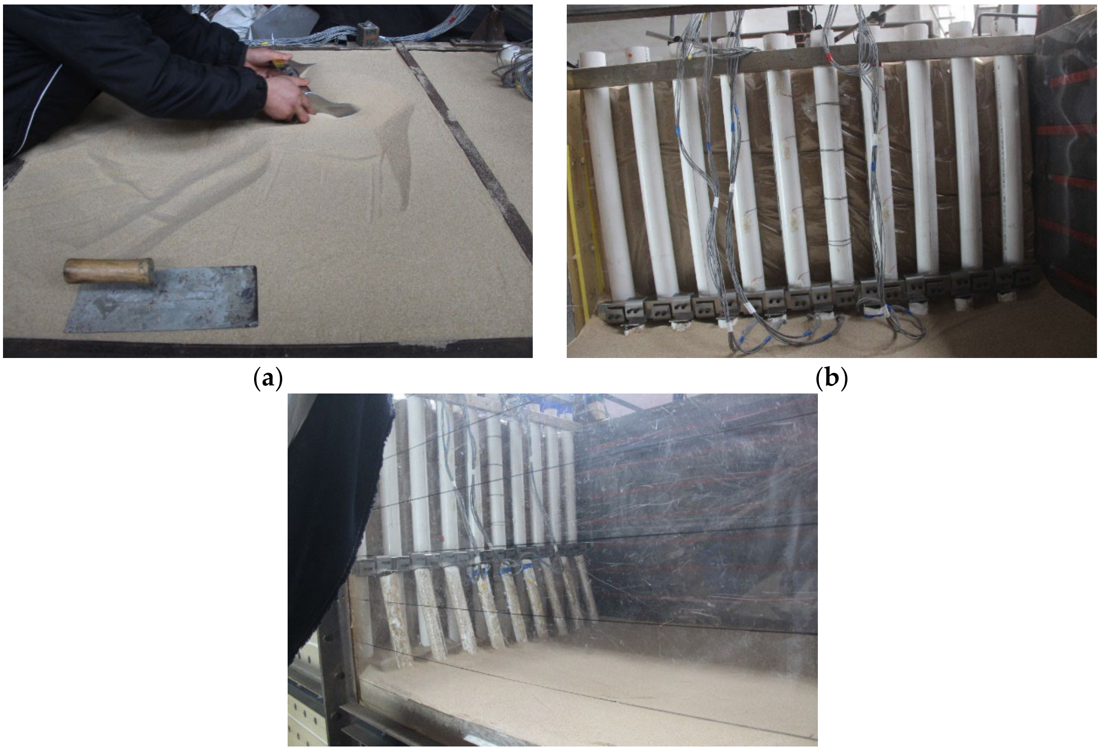
(**a**) (**b**) (c)

Figure 19. Process of excavation: (**a**) Excavation of foundation pit; (**b**) Connection between wale and inclined pile; (**c**) Completion of excavation.

3. Analysis of Test Results

3.1. Deformation of Vertical Pile

Figure 20 presents the results obtained for the deflection of the vertical piles in Groups R0-R5. Collapse happened while the excavation depth is 80 cm in Group R0, and the final displacements of vertical piles exceeds the measuring range of the dial indicators on the side of the model box. Thus, its deflection didn't be recorded, as shown in Figure 20(a).

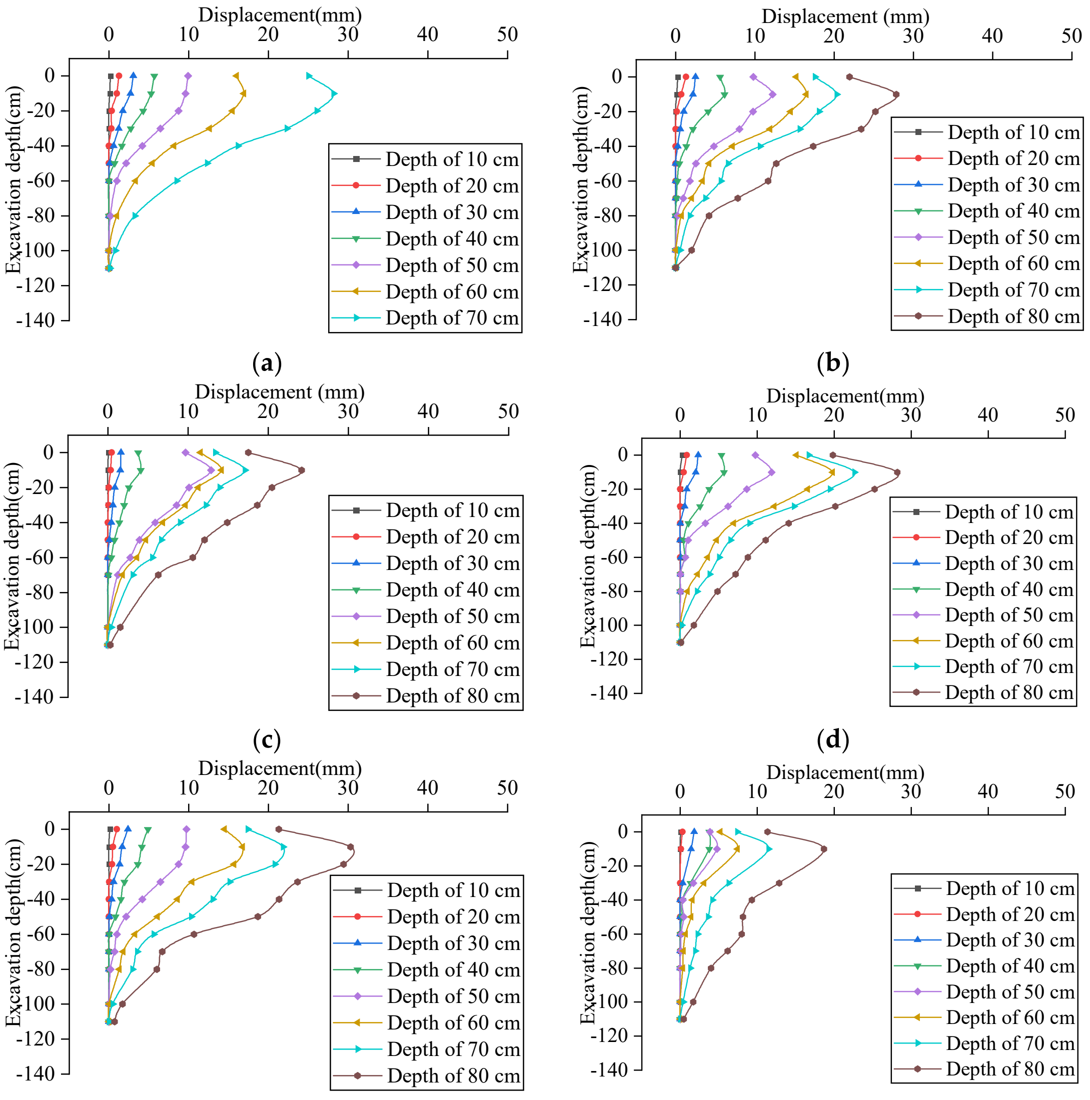

(**a**) (**b**)

(**c**) (**d**)

(**e**) (**f**)

Figure 20. Horizontal displacement distribution of the vertical piles for different excavation depths: (**a**) R0; (**b**) R1; (**c**) R2; (**d**) R3; (**e**) R4; (**f**) R5.

It can be seen from Figure 20 that the deformation of the vertical piles in Groups R0-R5 all gradually increased during excavation, even though the excavations with different retaining structures. The maximum deformation developed at the pile top and the deformation performed as triangular distribution in Group R0 (see Figure 20(a)). However, the lateral deformation presents two stages during excavations in Groups R1–R5: (i) when the sand was removed from ground level to H_1 (where the wale is installed), the lateral deformation distribution exhibited a triangular pattern, similar to that of the cantilever retaining structure-protected excavation in Group R0; (ii) when the sand was removed from H_1 to the excavation bottom (ranging from -50 cm to -80 cm in Groups R1–R4 and from -40 cm to -80 cm in Group R5), the deflection of the vertical piles at the position 10 cm below the wale tended to show a local convexity toward the pit. The lateral deformation thus showed a combination of triangular and parabolic distributions.

Comparing Figure 20(a) with Figure 20(b) to Figure 20 (f), it is clear that the lateral deformation in Group R0 is larger than those in Groups R1–R5, during removing sand of -50 cm to -80 cm. Figure 21 presents the lateral deformation at the top of vertical pile for different groups. The results depicted in Figure 21 indicate that the lateral deformation at the vertical pile head increased during the excavation process in Group R0. The lateral deformation increase significantly, with an increment of 46.9 mm during the excavation of -70 cm to -80 cm soil layer, accounting for 70.4% of the final deformation (71.7 mm). However, the increments of lateral deformation in Groups R1–R5 are smaller than that in Group R0. The final deformations of Groups R1–R5 are 22.0 mm, 17.5 mm, 19.8 mm, 21.3 mm, 11.3 mm, accounting for 30.68%, 24.41%, 27.62%, 29.71%, 5.76% of that in Group R0, respectively. The comparison reveals that VIPW can effectively control the lateral deformation induced by the excavation process to make the excavation safe.

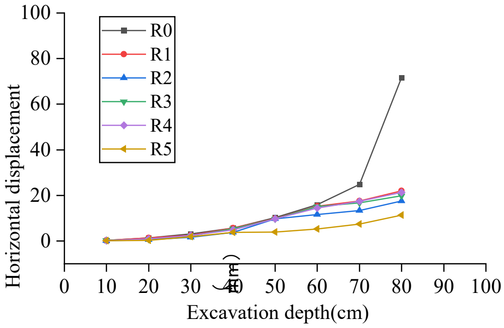

Figure 21. Horizontal displacements at the top of vertical piles for different groups.

It can also be observed that the increment of lateral deformation in Group R5 is smaller than that in the other groups, when excavated the -40 cm to -80 cm soil layer. This indicates that the inclined piles start to work after removing soil below -40 cm. A similar phenomenon also occurred in Groups R1–R4. The inclined piles started to work after removing soils below -50 cm in Group R2, while they did after removing soils below -60 cm in Groups R1, R3 and R4.

It is concluded that, the final lateral deformation is arranged in ascending order as $H_{dR5}<H_{dR2}<H_{dR3}<H_{dR4}<H_{dR1}<H_{dR0}$. Raising the supporting position of inclined piles or increasing the length of their embedded depth can improve the deformation control ability of VIPW. Increasing the embedded depth of vertical piles may have little effect on improving the deformation resistance of VIPW.

3.2. Surface Settlement

Figure 22 presents the results obtained for the surface settlement in Groups R0-R5. It can be seen that the distributions of surface settlement in different tests are similar. The settlement is larger in the area near the pit than that some distance away from the edge of the pit, developing as triangular distribution. The settlement in Group R0 increase significantly when removed the soil layer from -70 cm to -80 cm. The settlement also developed in two stages, consistent with the lateral deformation: (i) when the sand was removed from ground level to H_1, only the vertical piles acted as a cantilever; (ii) when the sand was removed from H_1 to the pit bottom, the VIPW functioned in this stage.

Figure 22(a) shows that the surface settlement increased significantly when removed soil layer of -70 cm to -80 cm in Group R0, similar to the lateral deformation. Comparing Figure 22(a) with Figure 22(b) to Figure 22(f), it is clear that the surface settlements in Groups R1–R5 are smaller than that in Group R0 in the second stage.

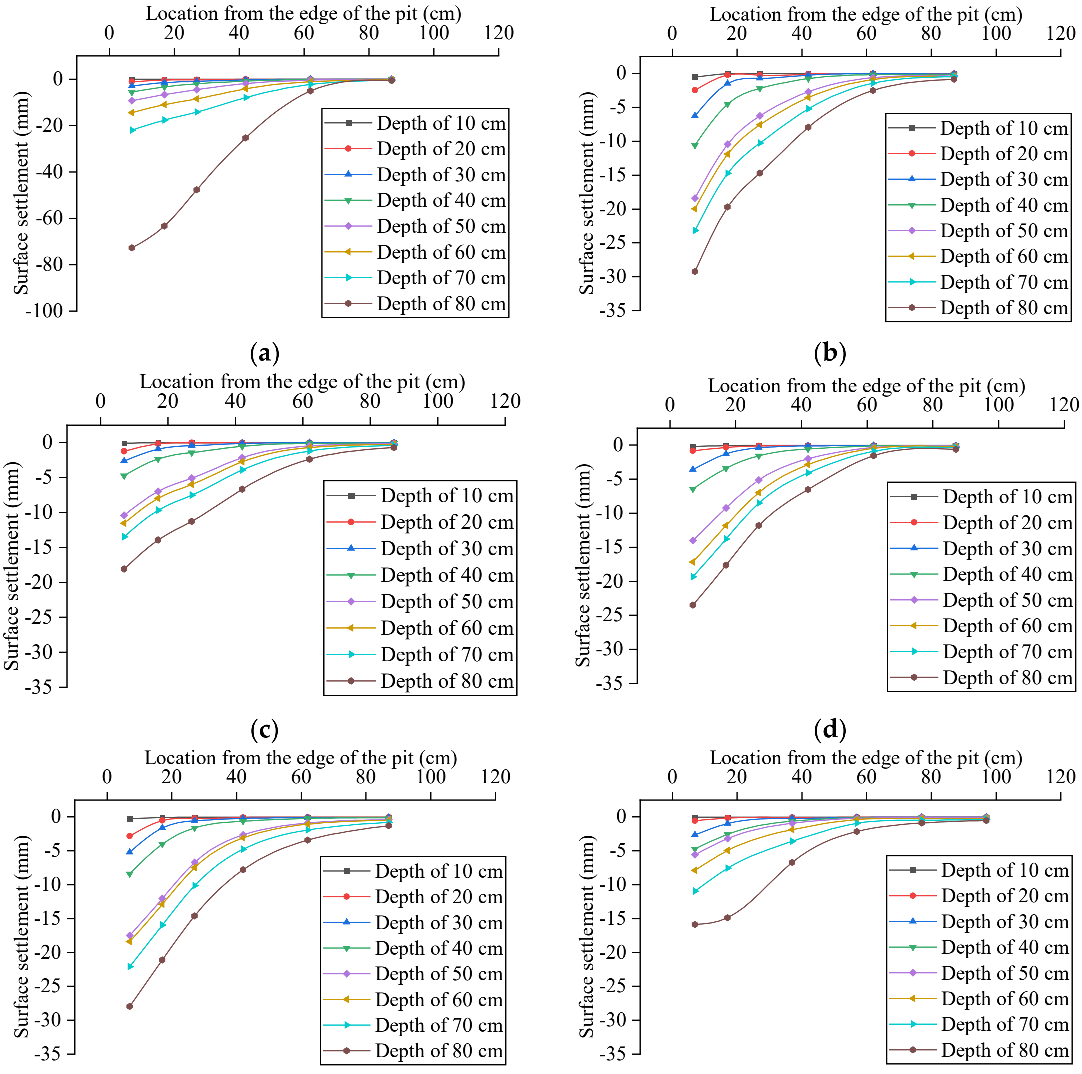

(a) (b)

(c) (d)

(e) (f)

Figure 22. Surface settlement for different excavation depths: (**a**) R0; (**b**) R1; (**c**) R2; (**d**) R3; (**e**) R4; (**f**) R5.

Figure 23 presents the settlement at the point 27 cm away from the edge of the pit in Groups R0-R5. As can be seen from Figure 23 that excavation phases lead to an increase in surface settlement. Surface settlement increases suddenly by 33.6 mm, 70.4% of the final settlement in Group R0. It implies that collapse happened in this process. However, Surface settlements in Groups R1–R5 are smaller than that in R0, and no sharp increase happened in the whole excavation processes. The final settlements of R1-R5 are 14.7 mm, 11.2 mm, 11.8 mm, 14.6 mm and 6.7 mm, respectively, accounting for approximately 30.8%, 23.6%, 24.7%, 30.6% and 14.1% of the settlement of Group R0. The comparison reveals that VIPW can effectively control the surface settlement induced by the excavation process.

It can also be observed that the surface settlement increments of Groups R1–R5 start to show differences, when excavated the soil layer below -40 cm. The increment of surface settlement in Group R5 is less than the other tests. The increment of surface settlement in Groups R1–R4 become small when excavated the soil layer below -50 cm. This phenomenon implies that the inclined piles start to work when excavated the soil layer below -40cm in Group R5, -50 cm in Groups R1–R4, respectively.

In conclusion, the order of surface settlement is $D_{R5} < D_{R2} < D_{R3} < D_{R4} < D_{R1} < D_{R0}$ when excavated the soil layer below -80 cm, which is consistent with the horizontal displacement distribution of the vertical piles described above. Therefore, appropriately increasing the supporting position of the inclined pile and increasing the depth from the excavation bottom to the tip of inclined pile can improve the deformation control ability of VIPW. Increasing the dip angle of inclined pile has little

doi:10.20944/preprints202603.1636.v1

effect on improving the ability of VIPW to resist deformation. Increasing the depth from the excavation bottom to the tip of vertical pile may not significantly improve the ability of VIPW to resist deformation.

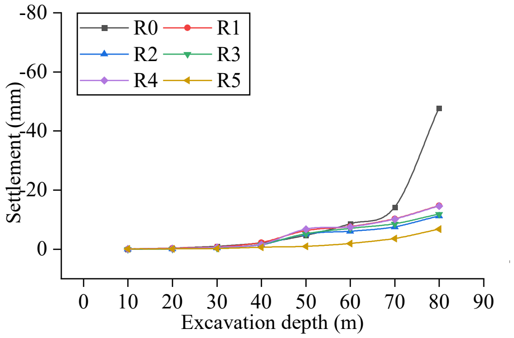

Figure 23. Surface settlement for different tests.

Due to space limitations, Figure 24-29 only show the surface conditions of Groups R0-R5 when the excavation depths are 70 cm and 80 cm. Figure 24 shows that in the Group R0, when the excavation depth is 80 cm, there are obvious sliding steps on the surface, and significant settlement deformation occurs near the edge of the excavation, indicating that the excavation is unstable. In the Groups R1–R5 (Figure 25 to 29), the surface settlement deformation is small, and there is no sliding step. It shows that with the increase of excavation depth, VIPW can effectively control the deformation of excavation and ensure the stability of excavation.

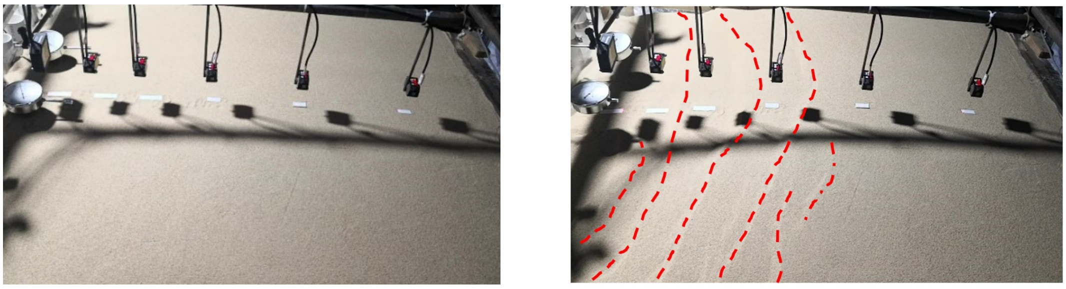

(**a**) (**b**)

Figure 24. Surface photos of R0 for different excavation depths: (**a**) The excavation depth is 70 cm; (**b**) The excavation depth is 80 cm.

(**a**) (**b**)

Figure 25. Surface photos of R1 for different excavation depths: (**a**) The excavation depth is 70 cm; (**b**) The excavation depth is 80 cm.


(**a**) (**b**)

Figure 26. Surface photos of R2 for different excavation depths: (**a**) The excavation depth is 70 cm; (**b**) The excavation depth is 80 cm.


(**a**) (**b**)

Figure 27. Surface photos of R3 for different excavation depths: (**a**) The excavation depth is 70 cm; (**b**) The excavation depth is 80 cm.


(**a**) (**b**)

Figure 28. Surface photos of R4 for different excavation depths: (**a**) The excavation depth is 70 cm; (**b**) The excavation depth is 80 cm.

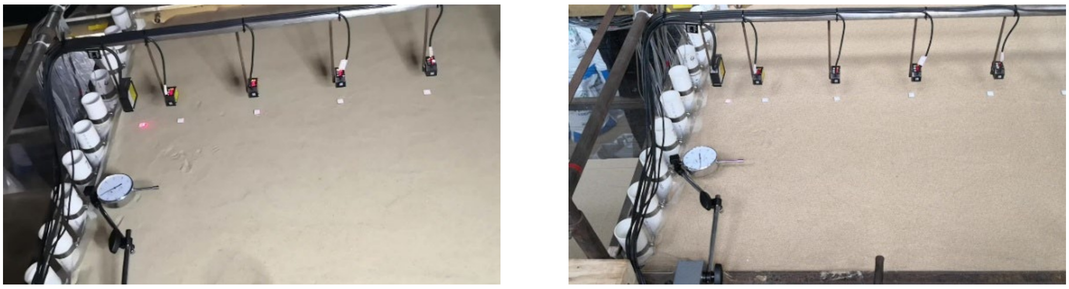
(**a**) (**b**)

Figure 29. Surface photos of R5 for different excavation depths: (**a**) The excavation depth is 70 cm; (**b**) The excavation depth is 80 cm.

3.3. Bending Moment of Vertical Pile

According to Table 6, the strains of the vertical piles were converted into the bending moments, and the bending moment distribution of the vertical piles during the excavation is shown in Figure 30. From Figure 30(a), it can be seen that the bending moment distribution of vertical pile in Group

R0 shows obvious parabolic characteristic. The maximum bending moment occurs in the range of 15-30 cm below the excavation surface, and gradually increases with the increase of excavation depth. When the excavation depth is greater than 50 cm, the bending moment value above the excavation surface will decrease. The reason for this phenomenon is that with the increase of excavation depth, the horizontal displacement of the vertical pile increases, the earth pressure behind the pile gradually changes from the static earth pressure to the active earth pressure, the settlement deformation of the top of the pit increases, and the effective depth of the soil layer in the active area behind the vertical pile decreases, as shown in Figure 30(b). The resultant force of earth pressure acting on the vertical pile in this area decreases, which leads to the decrease of the bending moment of the vertical pile in the range above the excavation surface. This phenomenon is consistent with the deformation characteristics of the pit above.

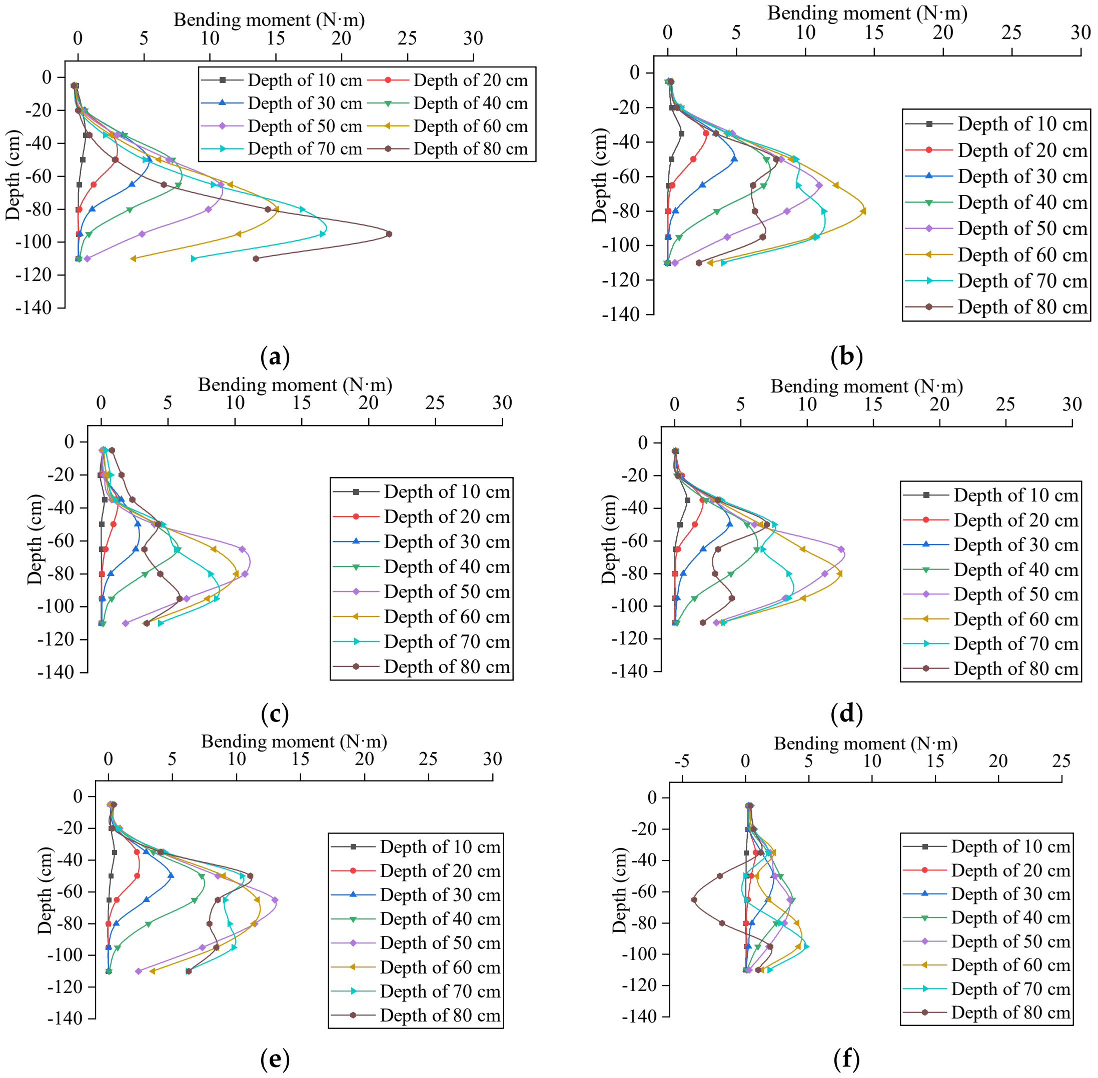

(**a**) (**b**) (**c**) (**d**) (**e**) (**f**)

Figure 30. Bending moment distribution of vertical piles for different excavation depths: (**a**) R0; (**b**) R1; (**c**) R2; (**d**) R3; (**e**) R4; (**f**) R5.

It can be seen from Figure 30(b) to (f) that the bending moment distributions of vertical piles in Groups R1–R5 are similar throughout the whole excavation process, which can be divided into two stages: (1) During excavation of the soil layer above the wale (50 cm for Groups R1–R4 and 40 cm for Group R5), the bending moment distribution characteristics of vertical piles are the same as those of R0, exhibiting the typical behavior of a cantilever retaining structure. With the increase of excavation depth, the bending moment values increase continuously, and the maximum bending moment occurs near the excavation surface or at a certain depth below it. (2) During excavation from the wale level down to the bottom of the foundation pit (80 cm depth), the maximum positive bending moment of the vertical piles gradually decreases; in other words, the bending moment values in the zone below the wale gradually decrease as the excavation depth increases. At the same time, there are three convex (concave) points in the bending moment curve during this process, which are as follows: (i) the first convex point is located at or near the wale (due to the distribution density of the measuring points, the position of R5 is 35 cm); (ii) the second concave point is located in the range of 15 cm to 25 cm below the wale (the positions of R1 to R4 are 65 cm, while that of R5 is 45 to 65 cm); (iii) the third convex point is located 15 to 20 cm below the excavation face in each excavation step.

Comparing Figure 30(a) with (b)–(f), it can be seen that when the excavation depth is greater than 50 cm, the bending moment values of the vertical piles in Groups R1–R5 are significantly smaller than those in R0. Therefore, it can be judged that due to the support force provided by the inclined pile, the bending moment distribution of the vertical pile is changed and the maximum bending moment value is reduced. In order to analyze the relationship between the bending moments of different groups during the excavation, the maximum bending moments of the vertical piles in each excavation step are selected as the analysis objects, and curves of maximum bending moment for each group of vertical piles under different excavation depths are drawn, as shown in Figure 31.

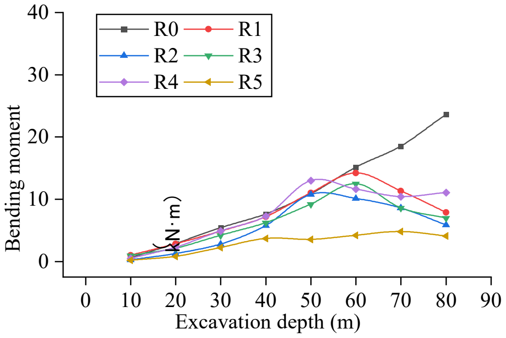

Figure 31. Maximum bending moment in vertical pile for different test.

From Figure 31, it can be observed that as the excavation depth increases, the maximum bending moment of the vertical piles in Group R0 continues to increase. When the excavation reaches the bottom (80 cm), the maximum bending moment is 23.6 N·m. In Groups R1–R5, when the excavation reaches 80 cm, the maximum bending moments of the vertical piles is significantly smaller than that in Group R0, and the final bending moments are 7.9 N·m (R1), 5.9 N·m (R2), 7.0 N·m (R3), 11.1 N·m (R4), and 4.1 N·m (R5), respectively. Notably, a point of contraflexure occurs in Group R5, resulting in a negative maximum bending moment, and the maximum bending moments in Groups R1–R5 are 33.5%, 25.0%, 29.7%, 47.0%, and 17.4% of the maximum bending moment in Group R0, respectively. It shows that the VIPW can improve the internal force distribution of the retaining structure and reduce its maximum bending moment value, which is conducive to the safety during the excavation process, and can reduce the reinforcement ratio of the retaining structure, thereby reducing costs.

Figure 31 also indicates that during the excavation of soil layers within 0–40 cm, the slope of the bending moment curve for the vertical pile in each group is similar and gradually increases. When the excavation depth exceeds 40 cm, differences gradually emerge among the maximum bending moment values of all test groups. The growth rate of the bending moment values in Group R5 significantly slows down and it is smaller than those in the other groups. Moreover, a negative bending moment occurs at an excavation depth of 80 cm, indicating that the inclined pile support in Group R5 effectively functions after reaching the 40 cm position. This provides a counteracting support force to the vertical pile, limiting its horizontal deformation and altering its internal force distribution. When the excavation depth reaches 50 cm for Groups R2 and R4, and 60 cm for Groups R1 and R3, the maximum bending moments of the vertical piles begin to decrease. This indicates that the inclined piles start to function, altering the distribution of internal forces. It can be observed that during the excavation process, the bending moment changes of the vertical piles in the VIPW from

doi:10.20944/preprints202603.1636.v1

Groups R1 to R5 are divided into two stages. The first stage involves excavating the soil layer from the ground surface to the wale, while the second stage involves excavating the soil layer from the wale to the pit bottom. In the first stage, the ground settlement deformation is the same as that of the cantilevered retaining structure model. In the second stage, the inclined piles and vertical piles form a herringbone retaining structure, working together, during which the maximum bending moments of the vertical piles gradually decrease.

In summary, when the excavation depth reaches the bottom (80 cm), the maximum bending moments of the vertical piles follow an ascending order: $M_{R5} < M_{R2} < M_{R3} < M_{R1} < M_{R4} < M_{R0}$. This trend is largely consistent with the previously observed patterns of horizontal deformation in the vertical piles and ground surface settlement. Increasing the support position of the inclined pile (Group R5) can enable them to provide stabilizing effects during the early stages of excavation, significantly improving the internal force distribution of the vertical pile. However, this adjustment may induce larger negative bending moment zone in the vertical pile. Enhancing the embedment depth of the inclined pile into the soil increases its bearing capacity, inherent stiffness, and stability, which effectively reduces the horizontal deformation of the herringbone pile retaining structure. Consequently, this approach also reduces the maximum bending moment value of the vertical pile.

3.4. Internal Force of Inclined Pile

During the excavation process, inclined piles experience complex mechanical behavior. When the pile head is rigidly connected to the wale, the pile head is subjected to a bending moment (M), axial force (N_1), and tangential force (T) from the wale. Along the pile shaft, the soil exerts normal forces (F_1, F_2) and tangential shear forces (τ_1, τ_2) on its surface, while the pile tip is loaded by a soil-induced axial force (N_2). A schematic diagram of these forces acting on the inclined pile is illustrated in Figure 32. Therefore, the strain values measured by strain gauge sensors represent the resultant strain caused by the combined forces at each measurement point. By conducting a mechanical analysis on any cross-section of the inclined pile, it is evident that the internal forces include bending moment, shear force, and axial force. Based on the principles of material mechanics, when the span of a beam exceeds five times its depth, the influence of shear force and lateral compressive stresses on the bending normal stress at any point of the cross-section can be neglected. The inclined piles used in texts have a length significantly greater than five times their diameter. Therefore, the bending normal stress on their cross-sections can be derived using the stress formula for a beam under pure bending [30]. Specifically, the maximum tensile stress and maximum compressive stress occur at two points located above and below the neutral axis, corresponding to the maximum tensile strain and maximum compressive strain, respectively. Under axial force, a uniformly distributed normal stress is generated across the cross-section, corresponding to axial tensile/compressive strain values. Under shear force, the cross-section undergoes relative shear deformation. Although this deformation is perpendicular to the outer surface of the inclined pile, strain gauges (which have a finite length along the axial direction of the pile) will still be affected by the shear-induced deformation, thereby influencing their measurement accuracy of axial strain values along the pile’s longitudinal axis. To simplify the analysis, it is assumed here that the influence of shear deformation (induced by shear forces) on the strain gauge measurements is negligible. Therefore, the strain values measured by the gauges are attributed solely to the tensile/compressive strains generated by the bending moment and axial force acting on the cross-section.

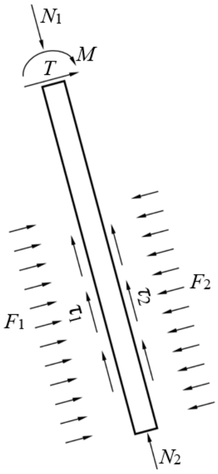

Figure 32. Stress diagram of inclined pile.

By selecting a cross-section of the inclined pile as the analytical subject and simplifying it to a hollow cylindrical member as shown in Figure 33(a), the section is subjected to a bending moment *M* and an axial force *N*. Under the combined action of these two loads, the member undergoes composite deformations, including axial compression (or tension) and bending deformation. Under the assumptions of linear elastic material behavior and small deformations, the stresses and deformations caused by the two types of loading can be calculated separately. The total stress and total strain on the cross-section can then be determined using the superposition principle. Specifically, the combined loading and deformation shown in Figure 33(a) can be decomposed into the superposition of the individual loading and deformation states illustrated in Figure 33(b) and 33(c). Assuming the strains at the edge points on both sides of the cross-section under the combined action of bending moment *M* and axial force *N* are ε_A and ε_B, respectively. Under the axial force *N* alone, the cross-section develops a uniformly distributed axial strain ε_x. Under the bending moment *M* alone, the edge points on both sides of the cross-section experience strains equal in magnitude but opposite in direction, denoted as $-\varepsilon_y$ and ε_y. Based on Hooke's law and the superposition principle, the formula for calculating the combined deformation of the cross-section can be derived as follows:

$$\varepsilon_A = \varepsilon_x - \varepsilon_y \tag{3}$$

$$\varepsilon_B = \varepsilon_x + \varepsilon_y \tag{4}$$

By combining Equations (3) and (4), the following can be derived:

$$\varepsilon_x = \frac{\varepsilon_A + \varepsilon_B}{2} \tag{5}$$

$$\varepsilon_y = \frac{\varepsilon_A - \varepsilon_B}{2} \tag{6}$$

Based on Equations (5)–(6) and the relationships between bending moment, axial stress, and strain at each measurement point provided in Table 7, the strain values measured at the inclined pile monitoring points during excavation are converted into bending moment *M* and axial stress σ. The axial force *N* is derived from the uniformly distributed axial stress σ as $N = \sigma \cdot A$, where *A* denotes the cross-sectional area of the inclined pile.

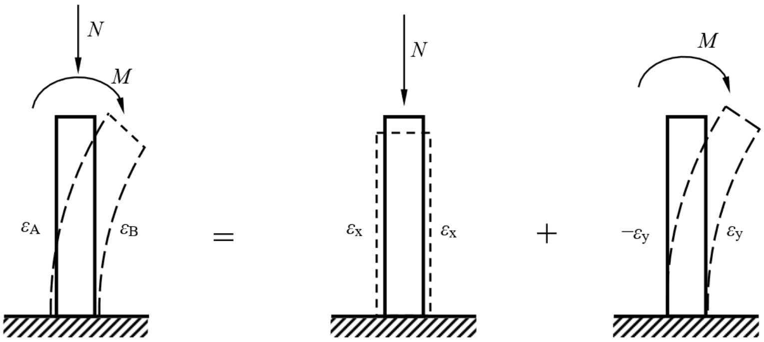

Figure 33. Stress and deformation in cross section of cylinder.

3.4.1. Bending Moment Distribution of Inclined Pile

The bending moment distributions of the inclined piles in each text group during the excavation are illustrated in Figures 34-38. A positive bending moment is defined as tensile stress developing at the lower side of the pile cross-section. Figures 34(a)–38(a) depict the variations in bending moment distributions of the inclined piles during the excavation of the soil layer from the ground surface to the wale. From the figures, it can be observed that during the shallow soil excavation phase, although the pile head and wale are in a separated state with no load transfer, positive bending moments (tensile stress at the lower side) are still induced in the inclined piles. Furthermore, the bending moment magnitude gradually increases as the excavation depth progresses. The observed phenomenon arises due to excavation-induced stress relief, which triggers inward lateral compression of the retaining piles toward the pit. The closer to the excavation face edges, the more obvious the compression. Simultaneously, the unloaded soil at the pit bottom rebounds, with greater rebound deformation occurring closer to the excavation boundary. The inclined piles experience combined upward and inward compressive forces, where the compressive effect at the pile head exceeds that at the tip, inducing a tendency for upward rotation about the inclined pile. Soil resistance restricts this rotation, generating a bending moment that produces tensile stress on the lower side of the pile, resulting in an upward concave deformation profile. During excavation to the wale level, the maximum bending moments of the inclined piles reached approximately 2.0 N·m (except for Group R5, which exhibited a lower value of 1.0 N·m), and no consistent pattern in bending moment variations was observed among the test groups.

During the excavation from the wale to the pit bottom, the tops of the inclined piles are connected to the wale, restricting the horizontal displacement of the vertical piles. Simultaneously, the vertical piles transmit loads through the wale, exerting compressive forces on the inclined piles. As shown in Figures 34(b)-38(b), as the excavation depth increases, the upper portion of the inclined piles develops progressively larger negative bending moments. Upon completion of excavation, the inclined piles exhibit an S-shaped deformation profile, characterized by an upward convex curvature in the upper segment and a downward convex curvature in the lower segment. This behavior stems from the combined effects of structural interactions and soil resistance. During soil excavation, the vertical piles undergo both flexural deformation and rotational displacement about a base pivot point, transmitting downward and inward loads to the inclined pile heads through the wale. The rigid connection between the inclined pile heads and the wale introduces additional bending moments from the wale's moment couple. Under these loads, upward convex deformation (negative bending moments) initiates at the inclined pile head. As the bending moment propagates downward along the pile axis, the lever arm effect causes a gradual transition to positive bending moments. This transition reflects the dominant influence of the horizontal load component from the wale compared to the vertical component. Simultaneously, the embedded lower portion of the inclined piles is constrained by lateral soil resistance, generating downward convex deformation (positive bending moments). This dual deformation mechanism–upward curvature at the top and downward curvature at the base—creates a self-stabilizing S-shaped bending moment distribution. The positive moments at the pile tip counteract rotational tendencies induced by horizontal loads, ensuring global stability without overturning.

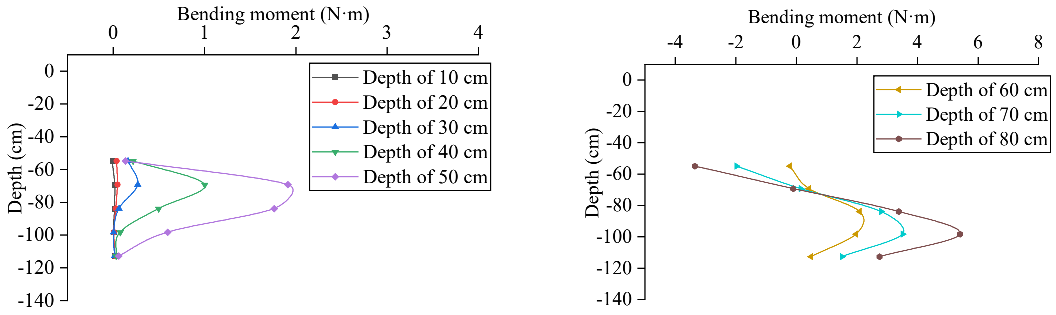

(**a**) (**b**)

Figure 34. Bending moment distribution of inclined pile in R1: (**a**) Before the inclined pile takes effect; (**b**) After the inclined pile takes effect.

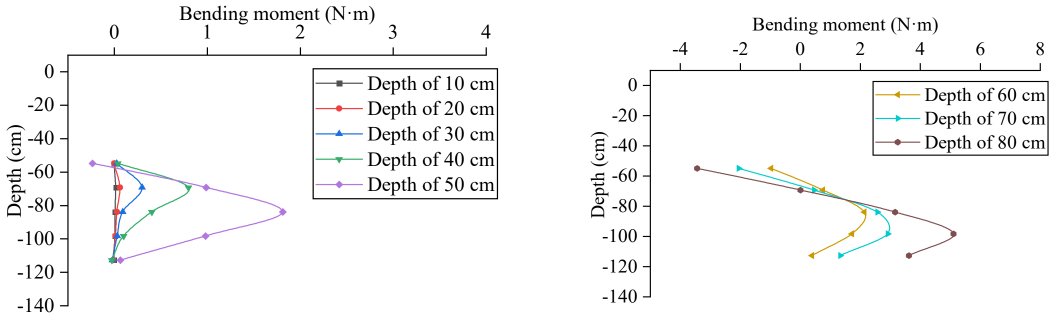

(**a**) (**b**)

Figure 35. Bending moment distribution of inclined pile in R2: (**a**) Before the inclined pile takes effect; (**b**) After the inclined pile takes effect.

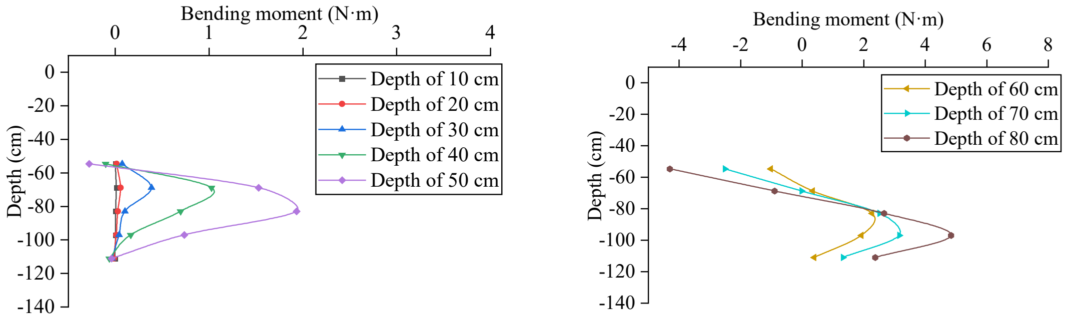

(**a**) (**b**)

Figure 36. Bending moment distribution of inclined pile in R3: (**a**) Before the inclined pile takes effect; (**b**) After the inclined pile takes effect.

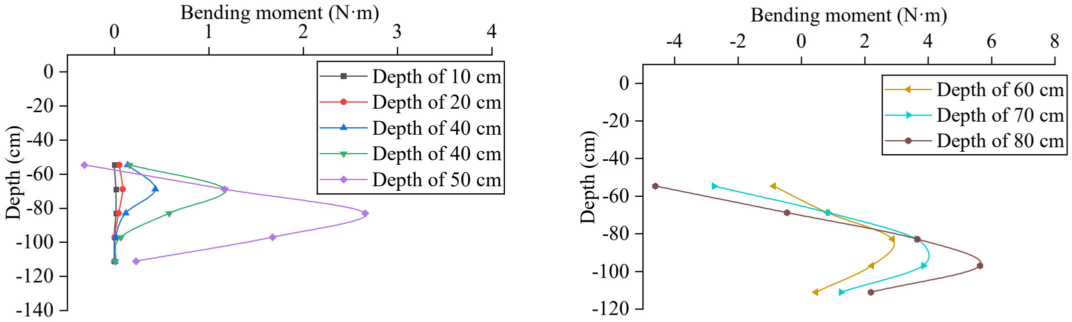

(**a**) (**b**)

Figure 37. Bending moment distribution of inclined pile in R4: (**a**) Before the inclined pile takes effect; (**b**) After the inclined pile takes effect.

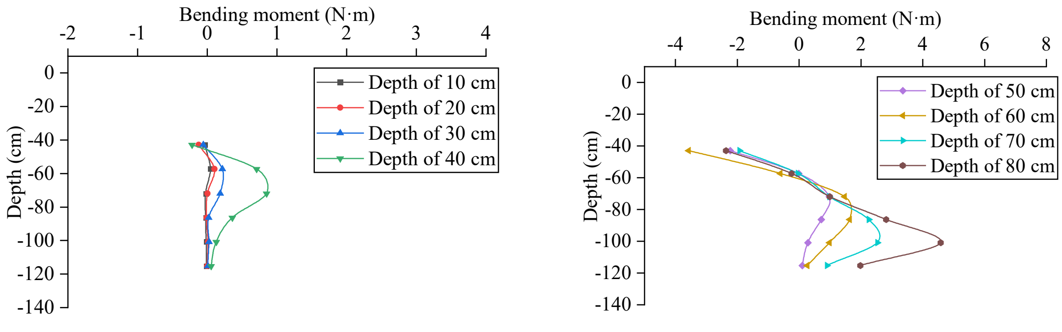

(**a**) (**b**)

Figure 38. Bending moment distribution of inclined pile in R5: (**a**) Before the inclined pile takes effect; (**b**) After the inclined pile takes effect.

Among the five test groups, during the excavation from the wale to the pit bottom (80 cm depth), the maximum negative bending moments at the pile heads exhibited incremental absolute values ranked as ΔMR5 (−1.18 N·m) < ΔMR2 (−3.20 N·m) < ΔMR1 (−3.67 N·m) < ΔMR3 (−4.01 N·m) < ΔMR4 (−4.28 N·m). Meanwhile, the maximum positive bending moments occurred at 18.30 cm below the pit bottom (20.85 cm for Group R5), with incremental magnitudes ascending as ΔMR1 (3.66 N·m) < ΔMR4 (3.96 N·m) < ΔMR3 (4.11 N·m) < ΔMR2 (4.13 N·m) < ΔMR5 (4.45 N·m). From the data above, it can be observed that raising the support elevation of inclined piles (R5) effectively reduced negative bending moments at the pile head but amplified positive bending moments along the shaft. In Group R2, the extended inclined pile length enhanced passive soil reinforcement, mitigating negative bending moments at the head while increasing positive moments along the shaft due to greater soil resistance. For Group R3, the larger inclination angle enlarged the lever arm of vertical force components from both the wale and pit bottom soil, intensifying both negative bending moments at the head and positive bending moments along the shaft. Conversely, Group R4, with longer vertical piles, exhibited the largest negative bending moment at the head and higher positive bending moments than Group R1, demonstrating that increasing vertical pile length fails to reduce maximum bending moments in inclined piles.

It can be seen from the above analysis that adjusting the geometric parameters of the herringbone retaining structure—such as raising the support position of inclined piles, extending the embedded depth of inclined piles, and increasing the inclination angle of inclined piles—can effectively reduce foundation pit deformation. However, this adjustment will increase the bending moment borne by the inclined piles. Additionally, increasing the embedded depth of vertical piles will also increase the maximum bending moment of inclined piles to a certain extent.

3.4.2. Axial Force Distribution of Inclined Pile

Figures 39–43 show the axial force distribution of inclined piles in each test group during the excavation process, with axial tension defined as positive. Figures 39(a)–43(a) depict the variations in axial force distributions of the inclined piles during the excavation of the soil layer from the ground surface to the wale. As can be seen from the figures, during the excavation of the shallow soil layer, although the top of the inclined pile is separated from the wale with no load transfer occurring, the inclined pile is still subjected to axial tension. Moreover, this axial tension gradually increases as the excavation depth increases. The reason for this phenomenon is that, due to the unloading caused by excavation, the soil layer below the excavation surface undergoes rebound deformation, generating an upward frictional force along the side of the inclined pile. This drives the inclined pile toward the excavation surface. The rebound deformation is more pronounced in areas closer to the excavation surface, resulting in greater displacement at the top of the inclined pile compared to the tip, thereby

Preprints.org (www.preprints.org) | NOT PEER-REVIEWED | Posted: 20 March 2026 doi:10.20944/preprints202603.1636.v1

subjecting the pile to axial tension. Simultaneously, the inclined pile itself rebounds due to the reduction in overburden pressure from the soil, leading to tensile strain. According to the stress-strain relationship, this is equivalent to the inclined pile being subjected to axial tension.

To analyze the variation law of the axial force of inclined piles after they are supported on the wale, a study was conducted on the variation law of the axial force of inclined piles during the process of excavating from the wale to the pit bottom in each group of tests, as shown in Figures 39(b)–43(b). It can be observed from the figures that in different groups, the axial force of the inclined piles gradually decreases from the excavation surface to the tip of the piles, which is consistent with the axial force distribution characteristics of building pile foundations. Furthermore, as the excavation depth increases, the axial force of the inclined piles gradually increases. When excavated to a depth of 80 cm, the axial loads at the tops of the inclined piles in each group were 194.19 N (R1), 193.52 N (R2), 170.79 N (R3), 185.00 N (R4), and 150.96 N (R5), respectively. When arranged in ascending order of magnitude, they follow the sequence: ΔNR5<ΔNR3<ΔNR4<ΔNR2≈ΔNR1. The axial load of the inclined pile in Group R5 is the smallest. In Group R3, as the inclination angle of the inclined pile increases, its horizontal component force increases. Therefore, the axial force it bears is smaller when the same supporting effect is achieved. For Group R4, owing to the greater embedded depth of the vertical pile, its deformation resistance is enhanced to some extent. Hence, compared with Group R1, the axial force of its inclined pile is slightly smaller. The axial forces of the inclined piles in Group R1 and Group R2 are approximately equal.

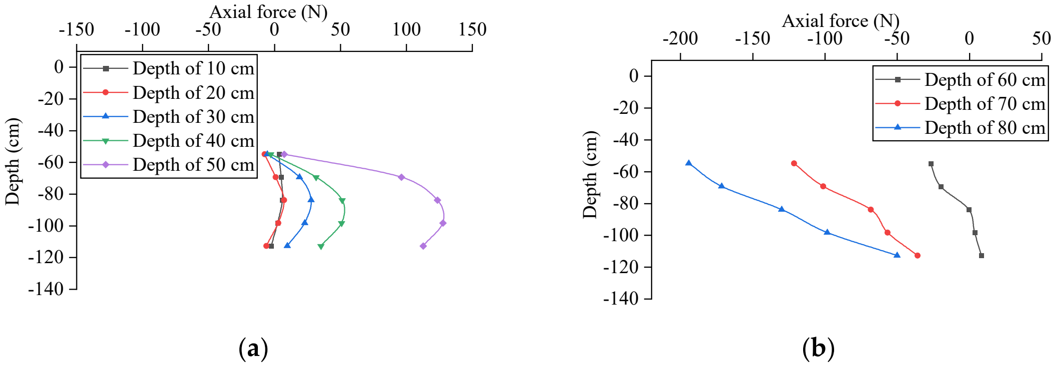

Figure 39. Axial force distribution of inclined pile in R1: (**a**) Before the inclined pile takes effect; (**b**) After the inclined pile takes effect.

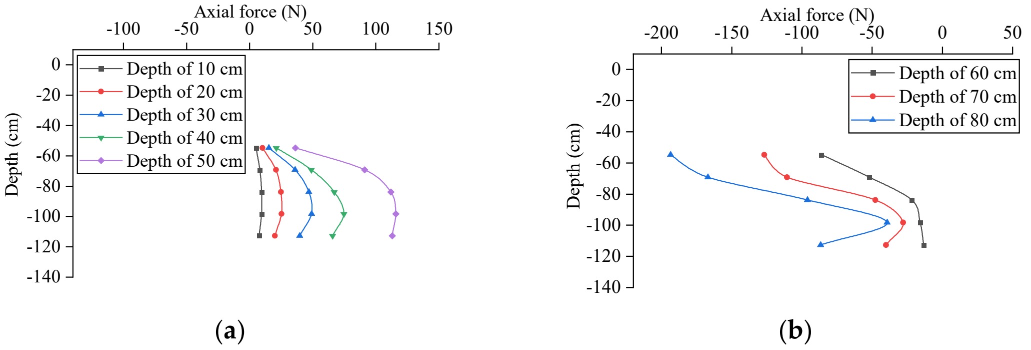

Figure 40. Axial force distribution of inclined pile in R2: (**a**) Before the inclined pile takes effect; (**b**) After the inclined pile takes effect.

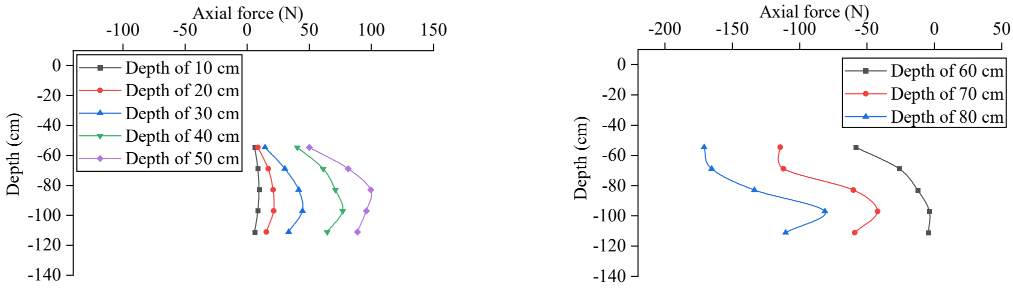

(**a**) (**b**)

Figure 41. Axial force distribution of inclined pile in R3: (**a**) Before the inclined pile takes effect; (**b**) After the inclined pile takes effect.

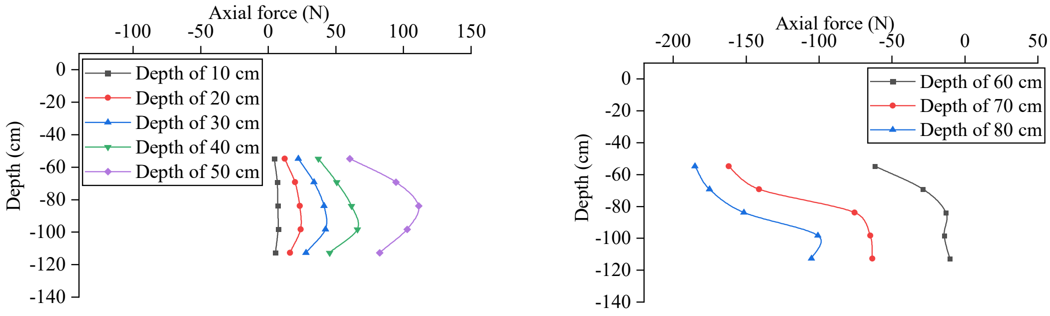

(**a**) (**b**)

Figure 42. Axial force distribution of inclined pile in R4: (**a**) Before the inclined pile takes effect; (**b**) After the inclined pile takes effect.

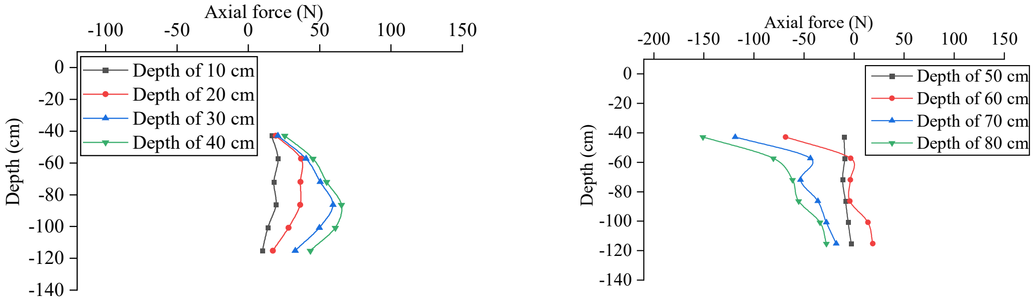

(**a**) (**b**)

Figure 43. Axial force distribution of inclined pile in R5: (**a**) Before the inclined pile takes effect; (**b**) After the inclined pile takes effect.

From the above analysis, it can be concluded that in the early stage of excavation, the pre-embedded inclined piles are affected by the unloading deformation of the soil layer at the pit bottom, thus generating a certain amount of tensile force. During the excavation process from the wale to the soil layer at the pit bottom, the axial forces of the inclined piles vary to a certain extent due to the different geometric forms of the herringbone retaining structure. Among these influencing factors, increasing the support position of the inclined piles enables the inclined piles to take effect in advance, resulting in a relatively smaller axial force. Additionally, increasing the inclination angle of the inclined piles can also reduce their axial force.

3.5. Unstable Failure Analysis

The previous analysis shows that in Group R0, the deformation of the foundation pit increased significantly when the soil layer was excavated to a depth of 60–70 cm, and a sudden change occurred when the excavation depth reached 70–80 cm. As can be seen in Figure 24(b), when the foundation pit in Group R0 was excavated to a depth of 80 cm, obvious sliding steps appeared on the ground surface. This indicates that the foundation pit suffered instability failure, and its safety could not be guaranteed. In Groups R1–R5, the deformation of the foundation pit was significantly smaller than that in Group R0, and no sudden deformation phenomenon occurred. To further study the effect of VIPW, this paper analyzes the lateral deformation of each group during the excavation from 50 cm to 80 cm, as shown in Figures 44-49.

As can be seen from Figure 44(c), when the foundation pit was excavated to a depth of 70 cm, discontinuous sliding failure surfaces appeared in the lateral soil of Group R0 (as indicated by the white dashed lines in the figures, the same below). This indicates that the foundation pit had a tendency to undergo instability failure at this point, that is, under the action of the cantilever supporting structure, the ultimate excavation depth of the foundation pit was less than 70 cm. As can be seen from Figure 44 (d), when the foundation pit is excavated to a depth of 80 cm, two continuous sliding failure surfaces appear in the soil on the side. The sliding surfaces are approximately triangular, which is consistent with the sudden change in the deformation shown in Figures 21 and 23. At this point, the foundation pit undergoes instability failure. The angle between the sliding surface and the horizontal plane is approximately 68.5°, which is slightly larger than the theoretical value of the sliding surface inclination angle of the soil layer under the active limit state (45+φ/2=64.4°). This phenomenon may be caused by factors such as the friction between the pile-soil interface and the friction between the side wall of the model box and the soil layer. As can be seen from Figures 45(d)-49(d), when the foundation pit is excavated to a depth of 80 cm, no sliding failure surface appears in the soil. This indicates that under the action of the VIPW structure, the ultimate excavation depth of the foundation pit is greater than 80 cm.

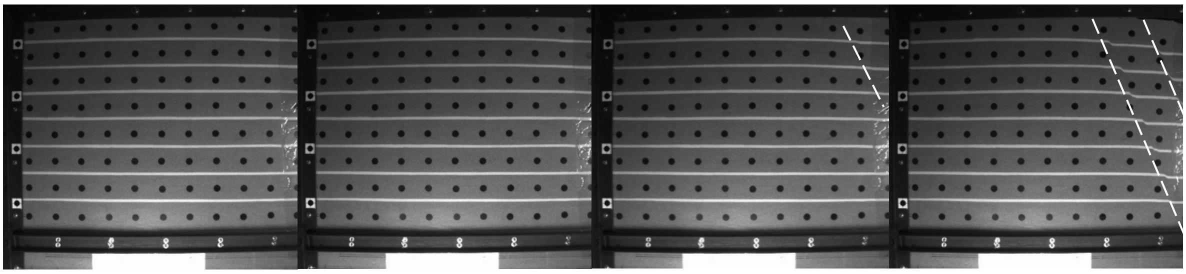
(**a**) (**b**) (**c**) (**d**)

Figure 44. Side face photos of R0 for different excavation depths: (**a**) Excavation depth of 50 cm; (**b**) Excavation depth of 60 cm; (**c**) Excavation depth of 70 cm; (**d**) Excavation depth of 80 cm.

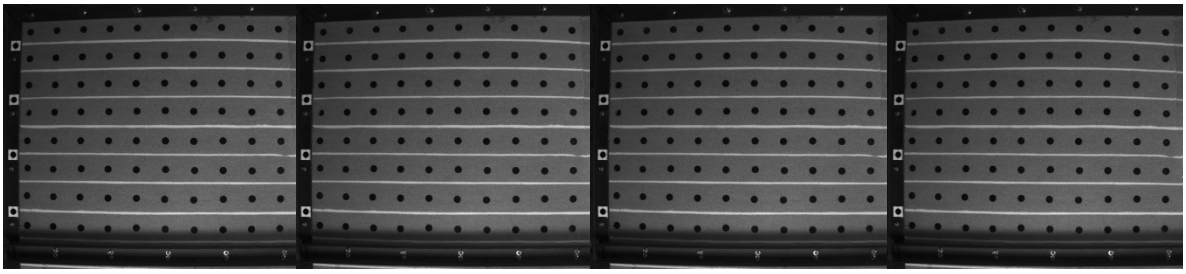
(**a**) (**b**) (**c**) (**d**)

Figure 45. Side face photos of R1 for different excavation depths: (**a**) Excavation depth of 50 cm; (**b**) Excavation depth of 60 cm; (**c**) Excavation depth of 70 cm; (**d**) Excavation depth of 80 cm.

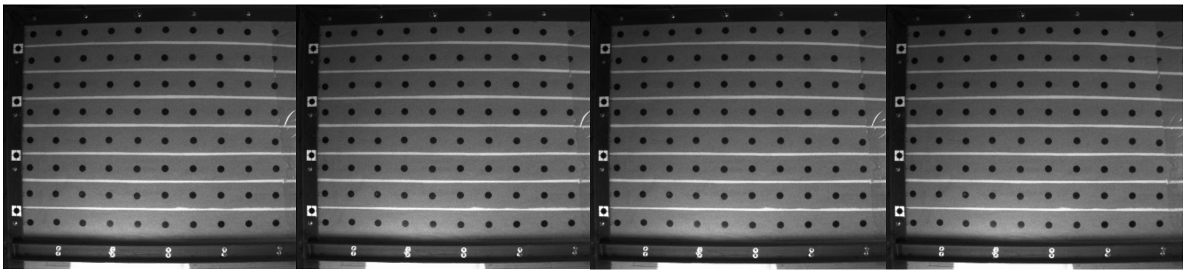
(a) (b) (c) (d)

Figure 46. Side face photos of R2 for different excavation depths: (**a**) Excavation depth of 50 cm; (**b**) Excavation depth of 60 cm; (**c**) Excavation depth of 70 cm; (**d**) Excavation depth of 80 cm.

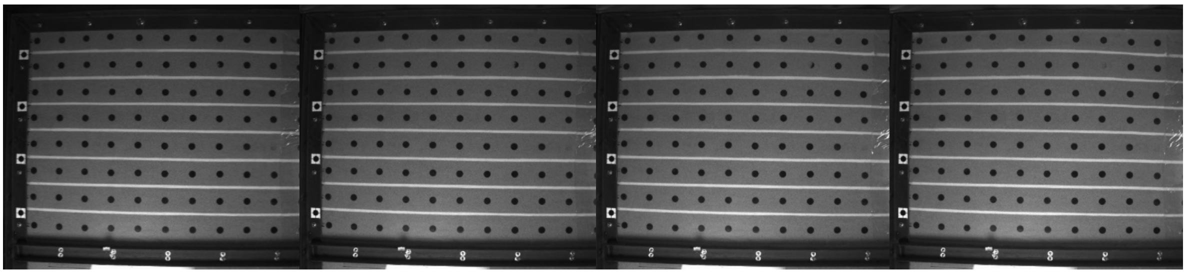
(a) (b) (c) (d)

Figure 47. Side face photos of R3 for different excavation depths: (**a**) Excavation depth of 50 cm; (**b**) Excavation depth of 60 cm; (**c**) Excavation depth of 70 cm; (**d**) Excavation depth of 80 cm.

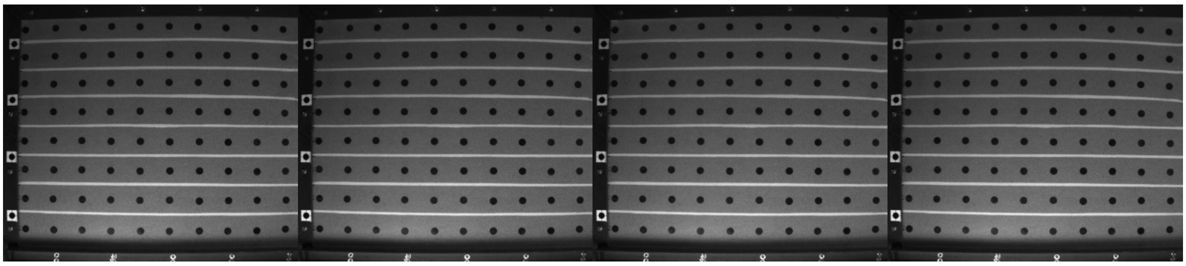
(a) (b) (c) (d)

Figure 48. Side face photos of R4 for different excavation depths: (**a**) Excavation depth of 50 cm; (**b**) Excavation depth of 60 cm; (**c**) Excavation depth of 70 cm; (**d**) Excavation depth of 80 cm.

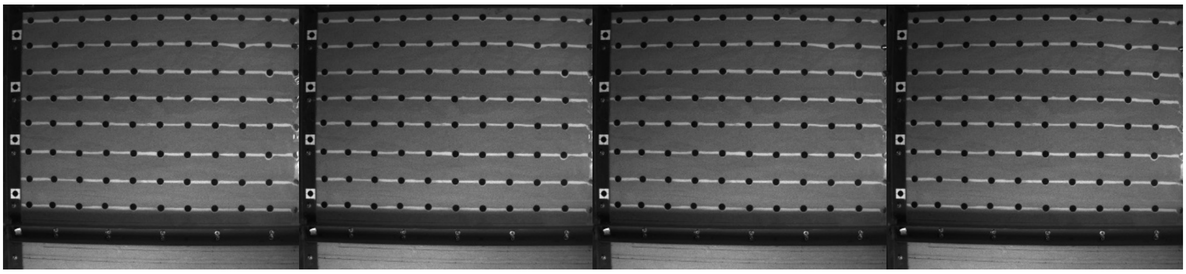
(a) (b) (c) (d)

Figure 49. Side face photos of R5 for different excavation depths: (**a**) Excavation depth of 50 cm; (**b**) Excavation depth of 60 cm; (**c**) Excavation depth of 70 cm; (**d**) Excavation depth of 80 cm.

In summary, under the action of the VIPW structure, the excavation depth of the foundation pit can be increased while ensuring safety and stability, and its supporting effect is far better than that of the cantilever supporting structure.

4. Conclusions

Large-scale physical model tests were conducted to investigate the deformation and mechanical characteristics of soldier pile wall (SPW) and vertical-inclined-piles wall (VIPW) for foundation pits, focusing on the influence of geometric parameters of support structures and revealing the action mechanism and stability-maintaining effect of VIPW. The main conclusions of this research are summarized below:

(1) Compared with SPW, the VIPW significantly reduced the horizontal displacement, surface settlement of the foundation pit, and the maximum bending moment of vertical piles. Specifically, the maximum deformation and bending moment of the optimal VIPW group (R5) are only 15.76% and 17.4% of those of the SPW group (R0). Additionally, the VIPW allows a stable excavation depth exceeding 80 cm without sliding failure surfaces in the external soil, whereas the SPW triggers discontinuous sliding surfaces at 70 cm excavation depth, demonstrating superior stability.

(2) In the VIPW system, the deformation and internal force evolution of vertical piles during excavation has two stages: before excavating to the wale, vertical piles show typical cantilever characteristics with maximum pile-top deformation and excavation-surface positive bending moment, both increasing with depth; after excavating below the wale, horizontal displacement growth slows, with a convex deformation 10 cm below the wale and an extreme bending moment at the wale, optimizing internal force distribution. The pit-top surface settlement presents a triangular distribution, with maximum settlement at the pit edge. For inclined piles, axial load is approximately triangularly distributed (maximum at the top), axial force increases with excavation depth, and bearing capacity transforms from side resistance-dominated to combined side and tip resistance. The rigid wale-inclined pile connection induces top negative bending moment and upward convex deformation, while the pit-bottom embedded segment generates positive bending moment due to lateral soil forces, preventing toppling and ensuring stability.

(3) Geometric parameters of the VIPW have different effects on its performance: increasing the brace position and embedment depth of inclined piles, as well as increasing the inclination angle of inclined piles, play significant roles in controlling foundation pit deformation and optimizing the bending moment distribution of vertical piles. In contrast, increasing the embedment depth of vertical piles has little effect or even an adverse impact. In summary, VIPW is a reliable foundation pit support scheme, which can provide technical reference for the design and construction of deep foundation pit engineering.

Author Contributions: Conceptualization, Haozhen Yue and Yapeng Zhang; Methodology, Yapeng Zhang; Validation, Haozhen Yue, Yapeng Zhang and Yun Zheng; Resources, Yun Zheng; Data curation, Haozhen Yue; Writing—original draft preparation, Haozhen Yue; Writing—review and editing, Haozhen Yue and Yapeng Zhang; Visualization, Chaoyi Sun; Supervision, Demin Xue; Funding acquisition, Chaoyi Sun and Demin Xue. All authors have read and agreed to the published version of the manuscript.

Funding: This research was funded by the Open Fund of State Key Laboratory of Geohazard Prevention and Geoenvironment Protection, grant number SKLGP2024K025 and the Natural Science Foundation of Wuhan, grant number 2025040601020179.

Data Availability Statement: The data that support the findings of this study are available from the corresponding author upon reasonable request.

Acknowledgments: The authors acknowledge the support from the following institutions: (1) Zhejiang Institute of Communications; (2) Zhejiang Engineering Research Center of Digital Highway Application Technology; (3) Zhejiang College of Construction; and (4) State Key Laboratory of Geomechanics and Geotechnical Engineering Safety, Institute of Rock and Soil Mechanics, Chinese Academy of Sciences.

Conflicts of Interest: The authors declare that they have no known competing financial interests or personal relationships that could have appeared to influence the work reported in this paper.

References

1. Zeng, F. Y.; Zhang, Z. J.; Wang, J. H.; Li, M. G. Observed performance of two adjacent and concurrently excavated deep foundation pits in soft clay. *J. Perform. Constr. Facil.* **2018**, *32*, 04018040. https://doi.org/10.1061/(Asce)Cf.1943-5509.0001184
2. Zhang, W.; Zhang, R.; Wang, W.; Zhang, F.; Goh, A. T. C. A multivariate adaptive regression splines model for determining horizontal wall deflection envelope for braced excavations in clays. *Tunn. Undergr. Space Technol*. **2019**, *84*, 461-471. https://doi.org/10.1016/j.tust.2018.11.046
3. Kok, S. T.; Huat, B. B. K.; Noorzaei, J.; Jaafar, M. S.; Gue, S. S. A case study of passive piles failure in open excavation. *DFI J*. **2009**, *3*, 49-56. https://doi.org/10.1179/dfi.2009.011
4. Öser, C.; Sayin, B. Geotechnical assessment and rehabilitation of retaining structures collapsed partially due to environmental effects. *Eng. Fail. Anal*. **2021**, *119*, 104998. https://doi.org/10.1016/j.engfailanal.2020.104998
5. Zhuang, Y.; Cui, X.; Hu, S. Numerical simulation and simplified analytical method to evaluate the displacement of adjacent tunnels caused by excavation. *Tunn. Undergr. Space Technol*. **2023**, *132*, 104879. https://doi.org/10.1016/j.tust.2022.104879
6. Zheng, G.; Lei, Y. W.; Cheng, X. S.; Li, X. Y.; Wang, R. Z. Experimental study on progressive collapse mechanism in braced and tied-back retaining systems of deep excavations. *Can. Geotech. J.* **2021**, *58*, 540-564. https://doi.org/10.1139/cgj-2019-0296
7. Zhang, W.; Heng, C.; Xu, C.; Zhou, Z.; Mao, L. Research on Support Technology of a soil-rock combination deep excavation in Qingdao. *KSCE J. Civ. Eng*. **2024**, *28*, 3208-3223. https://doi.org/10.1007/s12205-024-2199-5
8. Su, T.; Zhou, Y.; Wang, Z.; Ye, S. Large scale model test study of foundation pit supported by pile anchors. *Appl. Sci.* **2022**, *12*, 9792. https://doi.org/10.3390/app12199792
9. Yu, Z. T.; Wang, H. Y.; Wang, W.; Ling, D. S.; Zhang, X. D.; Wang, C.; Qu, Y. H. Experimental and numerical investigation on the effects of foundation pit excavation on adjacent tunnels in soft soil. *Math. Probl. Eng.* **2021**, *2021*, 5587857. https://doi.org/10.1155/2021/5587857
10. Yi, F.; Zheng, G.; Cheng, X.; Huang, T.; Jia, J.; Wang, Z. Progressive collapse analysis of the corner strut subsystem in a propped excavation with inadequate system safety performance. *Eng. Fail. Anal.* **2024**, *160*, 108231. https://doi.org/10.1016/j.engfailanal.2024.108231
11. Wang, S.; Li, Q.; Dong, J.; Wang, J.; Wang, M. Comparative investigation on deformation monitoring and numerical simulation of the deepest excavation in Beijing. *Bull. Eng. Geol. Environ.* **2021**, *80*, 1233-1247. https://doi.org/10.1007/s10064-020-02019-y
12. Mao, Z.; Ding, T.; Hu, F.; Ye, S.; Ding, L.; Shu, R.; Song, M. The deformation characteristics and patterns of adjacent existing metro structures caused by foundation pit excavation under different support forms. *Buildings* **2025**, *15*, 4178. https://doi.org/10.3390/buildings15224178
13. Zhang, W.; Zhang, R.; Fu, Y.; Goh, A. T. C.; Zhang, F. 2D and 3D numerical analysis on strut responses due to one-strut failure. *Geomech. Eng*. **2018**, *15*, 965-972. https://doi.org/10.12989/gae.2018.15.4.965
14. Zheng, G.; He, X.; Zhou, H.; Diao, Y.; Li, Z.; Liu, X. Performance of inclined-vertical framed retaining wall for excavation in clay. *Tunn. Undergr. Space Technol*. **2022**, *130*, 104767. https://doi.org/10.1016/j.tust.2022.104767
15. Fang, J.; Lin, S.; Liu, K. Multi-scale study of load-bearing mechanism of uplift piles based on model tests and numerical simulations. *Sci. Rep*. **2023**, *13*, 6410. https://doi.org/10.1038/s41598-023-33221-z
16. Qiu, H.; Zhou, Y.; Ayasrah, M. M. Impact study of deep foundations construction of inclined and straight combined support piles on adjacent pile foundations. *Appl. Sci.* **2023**, *13*, 1810. https://doi.org/10.3390/app13031810
17. Zheng, G.; Wang, Y.; Zhang, P.; Cheng, X.; Cheng, W.; Zhao, Y.; Li, X. Performances and working mechanisms of inclined retaining structures for deep excavations. *Adv. Civ. Eng*. **2020**, *2020*, 1740418. https://doi.org/10.1155/2020/1740418
18. Zheng, G.; Guo, Z.; Zhou, H.; Yu, D.; Wang, E.; He, X.; Liu, Z. Parametric studies of wall displacement in excavations with inclined framed retaining walls. *Int. J. Geomech.* **2022**, *22*, 04022157. https://doi.org/10.1061/(ASCE)GM.1943-5622.0002499

19. Zheng, G.; Liu, Z. P.; Zhou, H. Z.; He, X. P.; Guo, Z. Y. (2022). Behaviour of an outward inclined-vertical framed retaining wall of an excavation. *Acta Geotech*. **2022**, *17*, 5521-5532. https://doi.org/10.1007/s11440-022-01571-z
20. Zheng, G.; Guo, Z.; Zhou, H.; Tan, Y.; Wang, Z.; Li, S. Multibench-retained excavations with inclined–vertical framed retaining walls in soft soils: observations and numerical investigation. *J. Geotech. Geoenviron. Eng*. **2024**, *150*, 05024003. https://doi.org/10.1061/JGGEFK.GTENG-11943
21. Gan, F.; Zheng, G.; Li, M.; Liu, J.; Zhou, H.; Cao, T.; Wang, H. Large-scale model tests on inclined steel pipe pile retaining structures upon excavation. *J. Rock Mech. Geotech. Eng*. **2025**. https://doi.org/10.1016/j.jrmge.2025.07.018
22. Wang, Y.; Cheng, X.; Zheng, G. Numerical analysis of soil deformation in the excavation with loose sand retained by inclined retaining piles. *Sci. Rep*. **2024**, *14*, 31434. https://doi.org/10.1038/s41598-024-83152-6
23. Xie, B. L.; Liu, Y. C.; Jiang, H.; Guo, H.; Li, B. B. (2025). Analysis of the stability of inclined and vertical form retaining walls under foundation excavation and surcharge loading: Experiments and numerical simulation. *Eng. Fail. Anal.* **2025**, 110295. https://doi.org/10.1016/j.engfailanal.2025.110295
24. Zhang, Y.; Chen, C.; Lei, M.; Zheng, Y.; Zhang, H.; Shao, Y. Preliminary numerical analysis of a novel retaining system in dry sandy soil and its first application to a deep excavation in Wuhan (China). *Appl. Sci.* **2020**, *10*, 2006. https://doi.org/10.3390/app10062006
25. Wei, S.; Liang, R.; Mei, G.; El Naggar, M. H.; Sun, L.; Jia, J.; Wu, W. Experimental investigation on the deformation characteristics of locking-steel-pipe (LSP) pile retaining structure during excavation in sand. *Undergr. Space* **2022**, *7*, 1098-1114. https://doi.org/10.1016/j.undsp.2022.02.005
26. Gibson, A. D. Physical scale modeling of geotechnical structures at one-G. *Caltech* **1997**.
27. Scott, R. F. Centrifuge modeling and technology: a survey. *Rev. Fr. Geotech.* **1989**, *48*, 15-34.
28. You, M. Q.; Su, C. D.; Gou, Y. Experimental study on strength and deformation characteristics of marble specimens with holes. *Chin. J. Rock Mech. Eng.* **2007**, 2420-2429.
29. Zhang, Y. P.; Zheng, X. G.; Jin, X. G. Stability analysis of jointed surrounding rock of twin tunnels with small spacing based on Hoek-Brown criterion. *Technol. Highw. Transp.* **2014**, 48-52, 57.
30. Yan, S. P. *Mechanics of Materials*. Science Press: Beijing, China, 2012.